Thermal effects on the wake of a heated circular cylinder operating in mixed convection regime

H. Hu[1]† **and M. M. Koochesfahani**[2]

[1] Department of Aerospace Engineering, Iowa State University, Ames, IA 50011, USA

[2] Department of Mechanical Engineering, Michigan State University, East Lansing, MI 48824, USA

The thermal effects on the wake flow behind a heated circular cylinder operating in the mixed convection regime were investigated experimentally in the present study. The experiments were conducted in a vertical water channel with the heated cylinder placed horizontally and the flow approaching the cylinder downwards. With such a flow arrangement, the direction of the thermally induced buoyancy force acting on the fluid surrounding the heated cylinder would be opposite to the approach flow. During the experiments, the temperature and Reynolds number of the approach flow were held constant. By adjusting the surface temperature of the heated cylinder, the corresponding Richardson number ($Ri = Gr/Re^2$) was varied between 0.0 (unheated) and 1.04, resulting in a change in the heat transfer process from forced convection to mixed convection. A novel flow diagnostic technique, molecular tagging velocimetry and thermometry (MTV&T), was used for qualitative flow visualization of thermally induced flow structures and quantitative, simultaneous measurements of flow velocity and temperature distributions in the wake of the heated cylinder. With increasing temperature of the heated cylinder (i.e. Richardson number), significant modifications of the wake flow pattern and wake vortex shedding process were clearly revealed. When the Richardson number was relatively small ($Ri \leqslant 0.31$), the vortex shedding process in the wake of the heated cylinder was found to be quite similar to that of an unheated cylinder. As the Richardson number increased to ∼0.50, the wake vortex shedding process was found to be 'delayed', with the wake vortex structures beginning to shed much further downstream. As the Richardson number approached unity ($Ri \geqslant 0.72$), instead of having 'Kármán' vortices shedding alternately at the two sides of the heated cylinder, concurrent shedding of smaller vortex structures was observed in the near wake of the heated cylinder. The smaller vortex structures were found to behave more like 'Kelvin–Helmholtz' vortices than 'Kármán' vortices, and adjacent small vortices would merge to form larger vortex structures further downstream. It was also found that the shedding frequency of the wake vortex structures decreased with increasing Richardson number. The wake closure length and the drag coefficient of the heated cylinder were found initially to decrease slightly when the Richardson number was relatively small ($Ri < 0.31$), and then to increase monotonically with increasing Richardson number as the Richardson number became relatively large ($Ri > 0.31$). The

† Email address for correspondence: huhui@iastate.edu

average Nusselt number ($\overline{Nu}$) of the heated cylinder was found to decrease almost linearly with increasing Richardson number.

Key words: buoyancy-driven instability, buoyant boundary layers, wakes

---

1. Introduction

An understanding of the flow around a bluff body is of great importance owing to its fundamental nature as well as its many related engineering applications. A circular cylinder is the most commonly studied bluff body. Despite its simple shape, a circular cylinder generates a wake that is dynamically complex. By varying the Reynolds number, a variety of flow patterns and vortex shedding characteristics in the wakes of circular cylinders have already been observed. Extensive reviews about the effects of Reynolds number on the flow pattern in the wake of an unheated circular cylinder have been given by Roshko (1954), Berger & Wille (1972), Oertel (1990), Williamson (1996) and Zdravkovich (1997).

The wake behaviour behind a heated cylinder is physically more complicated owing to the thermal effects added to the viscous phenomena. As described in the textbook of Incropera & Dewitt (2001), heat transfer from a heated cylinder to the surrounding fluid can be either forced convection, mixed convection or pure free convection, depending on the ratio between the thermally induced buoyancy force and the inertial force, characterized by the Richardson number ($Ri = Gr/Re^2$, where Gr is the Grashof number and Re is the Reynolds number). In forced convection ($Ri \ll 1$), where the effect of the thermally induced buoyancy force is negligible, heat transfer is a function of Reynolds number and Prandtl number (Pr). In free convection ($Ri \gg 1$), where the flow inertial force is negligible, heat transfer is a function of Grashof number (Gr) and Prandtl number (Pr). In mixed convection, both forced convention and free convection are important, and heat transfer is a function of Grashof number (Gr), Reynolds number (Re) and Prandtl number (Pr) as well as the approaching forced flow direction. Despite the fact that mixed convection around bluff bodies is of great importance for various engineering applications such as electronics cooling, micro heat exchangers and fuel cells, the thermal effects on the wake flow behaviour behind a bluff body in the mixed convection regime have received little attention compared to those in the forced or free convection regimes.

When a heated cylinder operates in the mixed convection regime, the thermally induced buoyancy force plays an important role in the flow behaviour in the wake. As shown in figure 1, for a horizontally placed heated cylinder, the free-stream approach flow can be either horizontal, vertically upward or vertically downward. Following the terminology used by Badr (1983, 1984), they are called horizontal cross-flow, parallel flow and contra-flow arrangements based on the angle between the approach flow direction and the thermally induced buoyancy force acting on the fluid surrounding the heated cylinder.

Most of the earlier studies on heated cylinders operating in the mixed convection regime were focused on the determination of the global effects of thermally induced flows on the heat transfer coefficients compared with those in the forced convection regime. Oosthuizen & Madan (1970, 1971) found that heat transfer coefficients could be influenced considerably by the thermally induced flows when the Richardson number (Ri) was larger than a critical value (i.e. $Ri > Ri_{cri}$). It was also found that
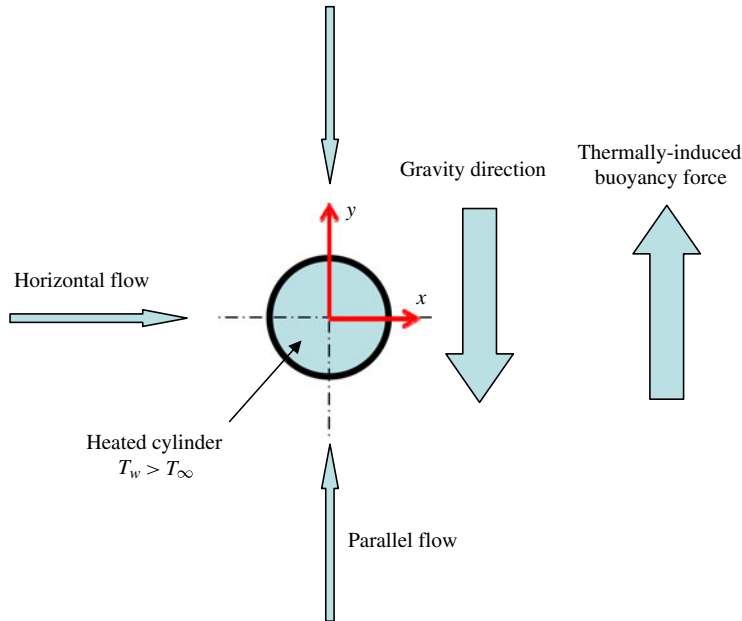
FIGURE 1. (Colour online available at journals.cambridge.org/flm) Schematic of forced flow arrangements around a heated cylinder with wall temperature T_w higher than the ambient temperature T_∞.

the value of the critical Richardson number would change with the angle between the approach flow direction and the thermally induced buoyancy force. Oosthuizen & Madan (1970, 1971) studied a heated circular cylinder placed in a horizontal, parallel and contra flow as well as 135° with respect to the thermally induced buoyancy force. They reported different critical Richardson numbers for different forced flow arrangements, and suggested that the heat transfer process around a heated cylinder would change from forced convection to mixed convection as the Richardson number becomes greater than the critical Richardson number.

Badr (1983, 1984) conducted his pioneering work on the numerical simulation of mixed heat convection from a heated cylinder to a laminar flow. He solved the coupled continuity, momentum and energy equations to study the mixed heat convection process from a heated, horizontally placed circular cylinder to a laminar horizontal, parallel or contra approach flow. Results, which include temperature fields and streamline patterns around the heated cylinder, were presented for $0 < Re < 40$ and $0 \leqslant Ri \leqslant 5$. The results revealed the significant changes of the wake flow structures behind the heated cylinder due to the thermal effects at different approach flow arrangements.

More detailed studies of the thermal effects on the wake behind a heated cylinder in the mixed convection regime were carried out slightly later, and some remarkable results were obtained. Noto, Ishida & Matsumoto (1985) studied the wake of a horizontally placed heated cylinder in a parallel flow, where the direction of the approach flow is vertically upward and parallel to the thermally induced buoyancy force (figure 1). By increasing the heat input (i.e. increasing Ri), the Strouhal number ($St = fD/U$) of the wake vortex shedding was found to increase at first. Then, the Strouhal number (St) became zero abruptly and the wake vortex shedding

process was suppressed when the Richardson number was above a critical Richardson number ($Ri_{cri} \approx 0.35$ for their study). The 'Kármán' vortex street downstream of the heated cylinder converted to two steady vortices situated in the near wake. A further increase of the heat input caused the twin vortices to disappear, ending with a thermal plume downstream of the heated cylinder. Chang & Sa (1990) conducted a numerical study to investigate the effects of the thermally induced buoyancy force on the wake vortex shedding for both parallel flow and contra-flow arrangements. Their numerical simulation of the parallel flow arrangement confirmed the findings of Noto *et al.* (1985). Similar results were also reported in the experimental study of Michaux-Leblond & Belorgey (1997), and the dualism between thermal effects and viscous effects was suggested to be responsible for the abrupt disappearance of the wake vortex shedding behind a heated cylinder exposed to a parallel approach flow.

More recently, Kieft, Rindt & van Steenhoven (1999) and van Steenhoven & Rindt (2003) studied the thermal effects on the wake behind horizontal heated cylinders exposed to horizontal cross-flow, where the direction of the approach flow is perpendicular to the direction of the thermally induced buoyancy force. They found that the non-parallelism between the approach flow direction and the buoyancy force caused the wake flow pattern to become asymmetrical, with the strength of the vortices in the upper vortex row being different from those in the lower row. The strength difference of the shedding vortices increased with increasing Richardson number (Ri). As a result, the shedding vortices were found to move slightly downwards, which is a rather unexpected behaviour considering the upward buoyancy force. Using an electrochemical tin precipitation method, Maas, Rindt & van Steenhoven (2003) visualized the wake structure behind a horizontally placed heated cylinder exposed to a horizontal approach flow. They found that the warmer fluid was initially collected in the coherent vortex structures shedding from the heated cylinder when the Richardson number was relatively small ($Ri < 1.0$). Thermal plumes were found to originate from the vortex structures further downstream. The Strouhal number of the vortex shedding behind the heated cylinder was found to increase as the Richardson number increased. For relatively large Richardson numbers ($Ri > 1.0$), the upward thermally induced buoyancy force prevented the formation of the coherent vortex structures and wake vortex structures became three-dimensional even near the rear end of the heated cylinder.

To the best of the authors' knowledge, very little can be found in the literature about the thermal effects on the wake flow behind a horizontal heated cylinder exposed to a contra-flow, where the direction of the approach flow is against the thermally induced buoyancy force. The numerical study of Chang & Sa (1990) may be the only available work that involves such a flow arrangement in the mixed convection regime. Instead of placing a heated cylinder in a vertically downward flow, Chang & Sa (1990) presented their numerical results (streaklines, streamlines and isothermal contours) for a cooled circular cylinder exposed to a vertically upward flow. They reported a decrease of the Strouhal number (St) of the wake vortex shedding, a reduction of the average Nusselt number ($\overline{Nu}$) and a decrease of the drag coefficient with the increase in temperature difference between the cooled cylinder and the approach flow.

In the present study, the thermal effects on the wake flow behind a horizontal heated circular cylinder exposed to a contra-flow are investigated experimentally. The experiments were conducted in a vertical water channel with the heated cylinder placed horizontally in the test section and the forced flow approaching the heated cylinder vertically downwards. The temperature and Reynolds number of the approach flow were held constant at $T_\infty = 24\,°C$ and $Re = \rho_\infty D U_\infty / \mu_\infty = 135$. The temperature

of the heated cylinder was varied between 24 °C (unheated cylinder) and 85 °C, corresponding to the Richardson number (Ri) varying between 0.0 (unheated) and 1.04. Over this range of Richardson number, the heat transfer process around the heated cylinder would change from the forced convection regime to the mixed convection regime.

A novel molecule-based flow diagnostic technique developed by the authors recently (Hu & Koochesfahani 2006), named molecular tagging velocimetry and thermometry (MTV&T), was used for qualitative flow visualization of the thermally induced flow structures and quantitative, simultaneous measurements of the velocity and temperature distributions in the wake of the heated cylinder. In the sections that follow, the basic technical aspects and system set-up of the MTV&T technique are introduced first. Then, the qualitative flow visualization images of the flow structures and the quantitative measurement results of the flow velocity and temperature distributions in the wake are presented. The thermal effects on the wake flow behind the heated cylinder are discussed in terms of the vortex shedding pattern, wake vortex shedding frequency (Strouhal number, St), the distributions of measured heat flux ($\overline{u_i'T'}$), the wake closure length (l_C), the drag coefficient (C_D) and the average Nusselt number ($\overline{Nu}$) of the heated cylinder. Preliminary results from this study were previously reported in a conference paper (Hu & Koochesfahani 2005). The present work adds much more detailed measurement results, extensive discussions and considerable analysis to elucidate the underlying flow physics.

2. Molecular tagging velocimetry and thermometry (MTV&T) technique

MTV&T is a molecule-based flow diagnostic technique, which can achieve both qualitative flow visualization of thermally induced flow structures and quantitative measurements of velocity and temperature distributions in fluid flows. Instead of using tiny tracer particles, MTV&T utilizes specially designed phosphorescent molecules, which can be turned into long-lived glowing markers upon excitation by photons of an appropriate wavelength. The water-soluble phosphorescent triplex (1-BrNp·Mβ-CD·ROH) was used in the present study as the molecular tracer for both flow velocity and temperature measurements. The properties and utilization of this tracer have been previously described (Ponce *et al.* 1993; Hartmann *et al.* 1996; Koochesfahani *et al.* 1996; Gendrich, Koochesfahani & Nocera 1997). Figure 2 shows the absorption spectrum and also the emission spectra of the phosphorescent triplex at different temperatures. It can be seen that the phosphorescence emission of this triplex is very temperature sensitive, whereas its fluorescence is not. The fluorescence lifetime of the triplex is within 20 ns, while its phosphorescence lifetime is ∼5.0 ms at 20 °C and decreases rapidly with increasing temperature (Hu & Koochesfahani 2003).

The MTV&T technique is actually an extension of the molecular tagging velocimetry (MTV) technique (Koochesfahani *et al.* 1996; Gendrich *et al.* 1997; Koochesfahani 1999; Koochesfahani & Nocera 2007). A pulsed laser is typically used to 'tag' the molecular tracers in the regions of interest, and those tagged molecules are interrogated at two successive times within the phosphorescence lifetime of the tracer. The measured Lagrangian displacements of the tagged molecules provide the estimate of the flow velocity vectors. The MTV technique can be considered as the molecular counterpart of particle image velocimetry (PIV) where fluid molecules, rather than seed particles, are marked and tracked. Figure 3 illustrates one implementation of the MTV technique. A planar grid of intersecting laser beams, formed from a pulsed ultraviolet (UV) laser, turns on the luminescence of the phosphorescent triplex
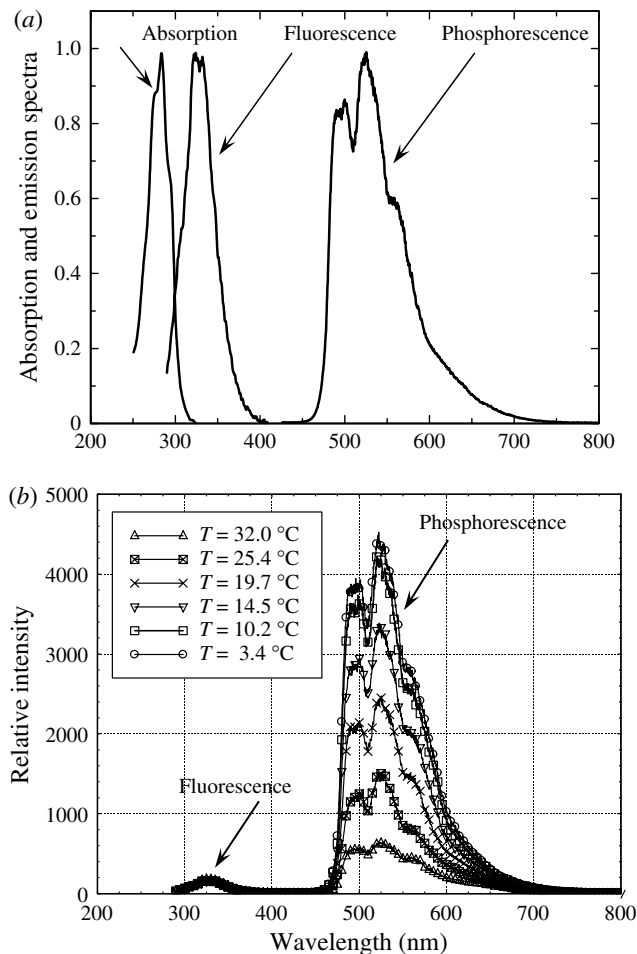
FIGURE 2. Absorption and emission spectra of the 1-BrNp·Mβ-CD·ROH triplex (Hu, Lum & Koochesfahani 2006): (*a*) normalized absorption and emission spectra at room temperature; (*b*) emission spectra at different temperatures (280 nm excitation of spectrophotometer).

molecules (1-BrNp·Mβ-CD·ROH) that are premixed in a water flow of a vortex ring approaching a solid wall at normal incidence (Gendrich *et al.* 1997). In the original work of Gendrich *et al.* (1997), for each laser pulse the MTV image pairs were acquired by a pair of aligned image detectors viewing the same region in the flow. In the present study, the two detectors are replaced by a single intensified charge-coupled device (CCD) camera (PCO DiCam-Pro) operating in dual-frame mode, which allows the acquisition of two images of the tagged regions with a programmable time delay between them. A direct spatial correlation method (Gendrich & Koochesfahani 1996) was used to determine the displacement of the tagged regions.

In addition to flow velocity field measurements, MTV&T can also provide simultaneous measurements of temperature distributions in the regions of interest by taking advantage of the temperature dependence of the phosphorescence lifetime of the tracer molecules (Hu & Koochesfahani 2003, 2006). According to quantum theory (Pringsheim 1949), the intensity of the photoluminescence process (either fluorescence or phosphorescence) decays exponentially. For a dilute solution and unsaturated laser
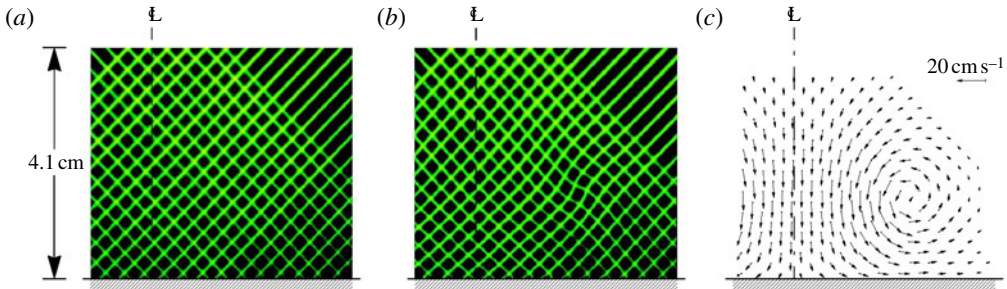
FIGURE 3. (Colour online) Typical MTV image pairs and the resultant two-dimensional velocity field (Gendrich *et al.* 1997). The flow shown is from a vortex ring impacting on a flat wall at normal incidence. The axis of symmetry is indicated by the dashed lines: (*a*) grid image 1 μs after the laser pulse; (*b*) same grid imaged 8 ms later; (*c*) velocity field derived from (*a*) and (*b*) (Gendrich *et al.* 1997).

excitation, the phosphorescence signal (S_p) collected by a gated imaging detector, with integration starting at a delay time t_o after the laser pulse and a gate period of δt, can be given by (Hu & Koochesfahani 2003; Hu *et al.* 2006, 2010)

$$S_p = A I_i C \varepsilon \Phi_p (1 - \mathrm{e}^{-\delta t/\tau}) \mathrm{e}^{-t_o/\tau}, \tag{2.1}$$

where A is a parameter representing the detection collection efficiency, I_i is the local incident laser intensity, C is the concentration of the phosphorescent dye (the tagged molecular tracer), ε is the absorption coefficient and Φ_p is the phosphorescence quantum efficiency. The emission lifetime τ refers to the time at which the intensity drops to 37 % (i.e. $1/e$) of the initial intensity.

In general, the absorption coefficient ε, quantum yield Φ_p and emission lifetime τ are temperature dependent (Ferraudi 1988), resulting in a temperature-dependent phosphorescence signal (S_p). Thus, in principle, the collected phosphorescence signal (S_p) may be used to measure the fluid temperature if the incident laser intensity and the concentration of the phosphorescent dye remain constant (or are known) in the regions of interest. Thermometry based on the laser-induced phosphorescence intensity of the phosphorescent triplex molecules, originally used by Thomson & Maynes (2001), is the phosphorescence version of the conventional laser-induced fluorescence (LIF) approach for thermometry. For accurate temperature measurements, however, the spatial and temporal variations of the incident laser intensity and the non-uniformity of the phosphorescent dye in the regions of interest would have to be corrected separately in order to derive quantitative temperature data from the acquired phosphorescence images. In practice, it is very difficult, if not impossible, to account for the *in situ* variations of the incident laser intensity distribution, especially for unsteady thermal flows with varying index of refraction. The measurements reported here rely, instead, on lifetime-based thermometry developed by Hu & Koochesfahani (2003, 2006), a ratiometric approach that eliminates the effects of incident laser intensity and concentration of the phosphorescent dye on temperature measurements.

Lifetime-based thermometry requires imaging the phosphorescence signal at two successive times, as in MTV measurements described earlier. As shown schematically in figure 4, the first image is detected at time $t = t_o$ after laser excitation for a gate period δt to accumulate the phosphorescence intensity S_1, while the second image is detected at time $t = t_o + \Delta t$ for the same gate period to accumulate the phosphorescence intensity S_2. It is easily shown, using (2.1), that the ratio of these two
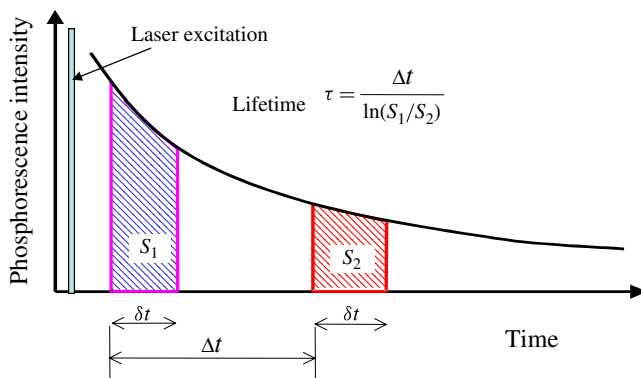
FIGURE 4. (Colour online) Calculation of phosphorescence lifetime from two successive images.

phosphorescence signals (R) is given by

$$R = \frac{S_2}{S_1} = e^{-\Delta t/\tau}. \tag{2.2}$$

In other words, the intensity ratio of the two successive phosphorescence images R is a function of only the phosphorescence lifetime τ and the time delay Δt between the image pair, which is a controllable parameter. This ratiometric approach eliminates the effects of any temporal and spatial variations in the incident laser intensity and non-uniformity of the dye concentration (e.g. due to bleaching). For a given molecular tracer and fixed Δt value, (2.2) defines a unique relation between phosphorescence intensity ratio R and fluid temperature T, which can be used for thermometry. The phosphorescence lifetime can be calculated according to

$$\tau = \frac{\Delta t}{\ln(S_1/S_2)}, \tag{2.3}$$

resulting in the distribution of the phosphorescence lifetime over a two-dimensional domain, and the temperature distribution in the flow as long as the temperature dependence of phosphorescence lifetime is known.

A calibration procedure (see Hu & Koochesfahani 2006) was conducted to obtain the quantitative relationship between the temperature and the phosphorescence lifetime of the phosphorescent triplex. Figure 5 depicts the measured phosphorescence intensity decay curves at different temperature levels and shows that they are well approximated by exponential curves, as expected theoretically. The calibration curve of the resulting phosphorescence lifetime versus temperature, shown in figure 6, illustrates that the phosphorescence lifetime of phosphorescent triplex (1-BrNp·Mβ-CD·ROH) varies significantly with temperature. The relative temperature sensitivity of the phosphorescence lifetime was found to vary between $5.0\%\ ^{\circ}\mathrm{C}^{-1}$ at $20\ ^{\circ}\mathrm{C}$ and $20.0\%\ ^{\circ}\mathrm{C}^{-1}$ at $50\ ^{\circ}\mathrm{C}$. We note that this temperature sensitivity is significantly higher than those of the commonly used LIF dyes. For comparison, the temperature sensitivity of Rhodamine B, the most commonly used dye in LIF-based thermometry, is $\sim 2.0\%\ ^{\circ}\mathrm{C}^{-1}$ (Hu *et al.* 2006). The enhanced temperature sensitivity of the LIF-based method, utilizing a two-colour, two-dye, approach with two temperature-sensitive fluorescent dyes of opposite temperature sensitivities, has been reported by Shafii, Lum & Koochesfahani (2010) to be $\sim 4\%\ ^{\circ}\mathrm{C}^{-1}$.
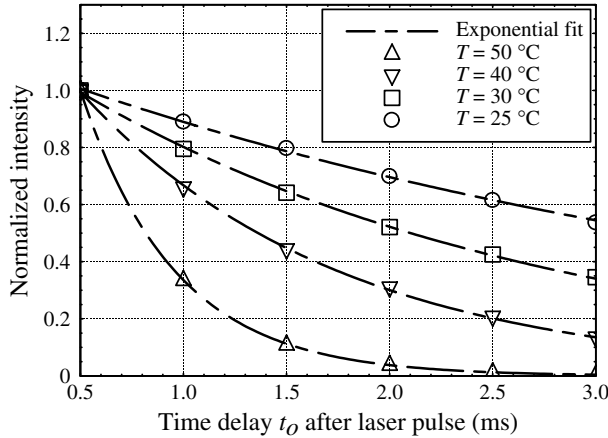
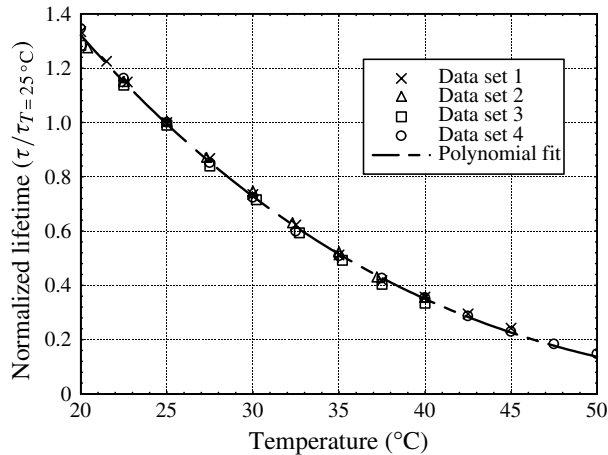FIGURE 5. Phosphorescence intensity decay curves at several temperature levels.

FIGURE 6. Variation of phosphorescence lifetime versus temperature.

In summary, the MTV&T technique achieves the simultaneous measurements of velocity and temperature by using a pulsed laser to 'tag' the tracer molecules in the regions of interest, and then interrogating them at two successive times within the phosphorescence lifetime. The measured Lagrangian displacements of the tagged tracer molecules provide the estimates of the velocity vectors. The simultaneous temperature measurement is achieved by taking advantage of the temperature dependence of the phosphorescence lifetime of the tagged tracer molecules, which is estimated from the intensity ratio of the two phosphorescence images.

It should be noted that the MTV&T technique, like most measurement techniques, does not give information at a 'point'. Rather, it provides the spatially averaged flow velocity and temperature of the molecularly tagged region. Similar to PIV, the effective spatial resolution of the measurement is given by the sum of the source window size and the measured Lagrangian displacement. For the results given in the present study, the spatial resolution was dominated by the source window size of 32×32 pixels (1.7 mm $\times 1.7$ mm in physical space, or $0.35D \times 0.35D$). Clearly, obtaining

spatially resolved data for small-scale flow structures would require tagging regions, and selecting interrogation windows, consistent with the scales to be resolved. While the best spatial resolution that can be achieved with MTV&T measurement is set by the diffraction limitations of the optics used to generate the tagging pattern and the resolution characteristics of image detection, the selection of the source (interrogation) window often involves a choice between the spatial resolution of the measurement versus the accuracy of the instantaneous measurement (see Hu & Koochesfahani 2006). The temporal resolution of the MTV&T measurements is set by the time delay Δt between the phosphorescence image pair, which in the present study was 5.0 ms. The choice of this time delay influences the accuracy of the velocity data (larger Δt leads to larger Lagrangian displacement of tagged tracer molecules) and the temperature estimation. It is worth noting that thermally induced distortions may cause errors in determining the positions of the measurement points, and the significance of these effects will depend on the scale of the measurement results given in the present study; the spatial resolution of the current MTV&T measurements is ~1.7 mm × 1.7 mm in physical space, while the scale of the thermally induced distortion was estimated to be less than 0.2 mm. Therefore, the effects of these distortions are believed to be negligible for the present study. However, such effects could become significant when the scale of the thermally induced distortions is comparable to the spatial resolution of the measurements, for example in cases with very large temperature gradients and/or very high spatial resolution. Further discussion of the effects of these factors on the flow velocity and temperature measurement accuracy by using the MTV&T technique is found in Gendrich & Koochesfahani (1996) and Hu & Koochesfahani (2006). For the measurement results given in the present study, the uncertainty in the measurement of the displacement of tagged regions is given by a 95 % confidence limit of ~±0.2 pixel, or root-mean-square (r.m.s.) accuracy of ±0.1 pixel, corresponding to an uncertainty of ~3 % in instantaneous flow velocity measurements. The uncertainty for the instantaneous temperature measurements is estimated to be ~±0.25 °C.

3. Experimental set-up and flow conditions

A schematic of the experimental set-up used for the present study is shown in figure 7. The test cylinder was installed horizontally in a gravity-driven vertical water channel. The dimensions of the test section were 50 mm (width) × 30 mm (height) × 200 mm (length). Quartz windows were made at the two sides of the test section to allow the transmission of an excimer UV laser light (wavelength $\lambda = 308$ nm). The 1-BrNp·Mβ-CD·ROH phosphorescent triplex was premixed with water in a reservoir tank, whose temperature was held fixed using a constant-temperature bath. A constant-head tank was used to maintain a steady inflow condition during the experiment. The constant-head tank was filled from the reservoir tank using an electric pump. A convergent section with honeycomb and mesh structures was used at the upstream of the test section to produce a uniform condition for the flow approaching the test cylinder. The velocity of the flow in the water channel was adjustable by operating the valve at the downstream end of the water channel.

A copper tube with outer diameter of $D = 4.76$ mm and inner diameter of 4.00 mm was used as the test cylinder. The cylinder was heated using a 3.1 mm diameter rod cartridge heater (Watlow Firerod) that was placed inside the copper tube. High-thermal-conductivity paste (Omegatherm 201) was pressed in to fill the gap between the rod cartridge heater and the inner wall of the copper tube. The rod cartridge heater was powered by a DC power supply (Kepco, BOP-200-2M). Two J-type thermocouples
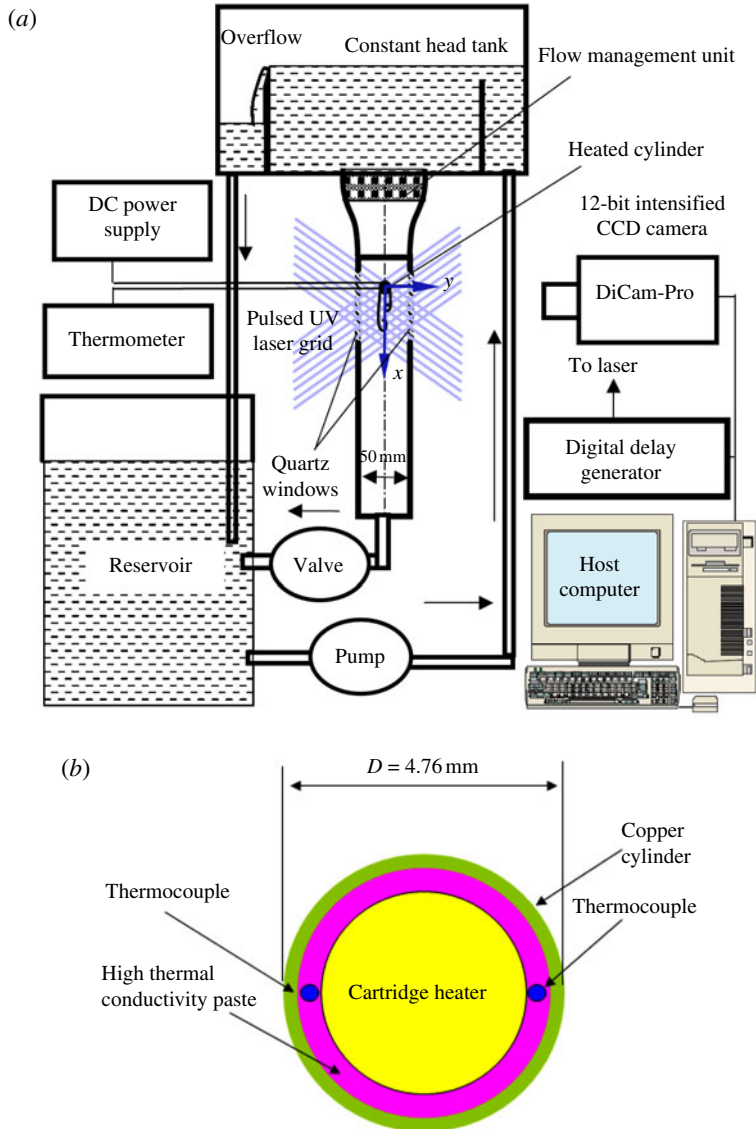
FIGURE 7. (Colour online) (*a*) Experimental set-up and (*b*) configuration of the heated cylinder.

were embedded in the gap at the mid-span of the cylinder at two angular locations to provide the estimate of the cylinder temperature (figure 7). The thermocouples were connected to a two-channel thermometer (Omega HH23), which had a resolution of $\pm 0.1\,^{\circ}\text{C}$.

In order to measure two components of the flow velocity in the wake of the test cylinder, a grid of intersecting laser lines were used for molecular tagging. Figure 8 shows the schematic of the optical set-up. A Lambda-Physik XeCl excimer laser (wavelength $\lambda = 308$ nm, energy 100 mJ pulse^{-1}, pulse width 20 ns) with appropriate optics was used to generate a laser sheet (thickness ~ 1 mm). The resulting laser sheet was split by a 50:50 beam splitter; each of the two resulting sheets passed through a
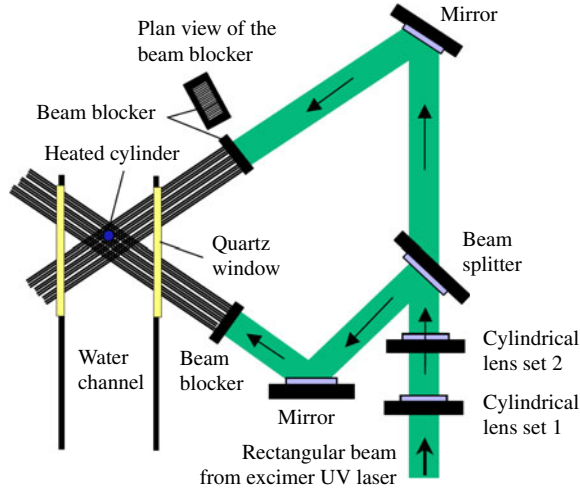
FIGURE 8. (Colour online) Schematic of the optical set-up.

beam blocker to generate the grid pattern. The beam blocker was simply an aluminium plate with a series of thin slots.

A 12-bit (1280 × 1024 pixels) gated intensified CCD camera (PCO DICAM-Pro) with a fast-decay phosphor (P46) was used for image recording. The camera was operated in the dual-frame mode, where two full-frame images of phosphorescence were acquired in quick succession from the same laser excitation pulse. For the measurement results given in the present study, the first images were captured at the time delay of 1.0 ms after the laser pulse, with the interrogation gate period of 0.5 ms. The second phosphorescence images were captured at the time delay of 6.0 ms after the laser excitation pulse, with the same interrogation gate period. The laser and the camera were synchronized using a digital delay generator (SRS-DDG535), which controlled the timing of the laser sheet illumination and the CCD camera data acquisition. The phosphorescence images captured by the CCD camera were subsequently transferred to a host computer for analysis.

During the experiments, the heated cylinder was placed horizontally in the middle of the water channel, and the forced flow was vertically downwards to approach the heated cylinder. Such an arrangement makes the heated cylinder operate in a contra-flow, i.e. the direction of the approach flow opposes the direction of the thermally induced buoyancy force. The velocity of the approaching forced flow, measured at ∼10 diameters upstream of the test cylinder, was 0.026 m s^{-1} ($U_\infty = 0.026$ m s^{-1}). The temperature of the forced flow in the constant-head tank was 24.0 °C ($T_\infty = 24.0$ °C). The corresponding Reynolds number was 135. The temperature of the test cylinder was set at six temperature levels, which varied from 24.0 °C (unheated cylinder) to 85.0 °C. The corresponding Grashof number changed from 0 to 19 000, representing a Richardson number variation between 0.0 and 1.04, along with a corresponding change in the heat transfer process from forced convection to mixed convection regime. The controlling parameters of the six studied cases are listed in table 1.

Case no.	T_w (°C)	T_∞ (°C)	Re	Gr	Ri
1	24	24.0	135	0	0.00
2	35	24.0	135	3 400	0.19
3	42	24.0	135	5 600	0.31
4	53	24.0	135	9 100	0.50
5	66	24.0	135	13 100	0.72
6	85	24.0	135	19 100	1.04

TABLE 1. The controlling flow parameters of the six cases studied. Grashof number, $Gr = g\beta(T_w - T_\infty)D^3/\nu_\infty^2$; Reynolds number, $Re = \rho U_\infty D/\mu_\infty$; Richardson number, $Ri = Gr/Re^2$.

4. Experimental results and discussion

4.1. *Qualitative flow visualization images and simultaneous flow velocity and temperature measurement results*

Figures 9(*a*) and 9(*b*) show a typical pair of phosphorescence images for the MTV&T measurements with the cartridge heater turned off (i.e. case 1). Compared with the phosphorescence image pair shown in figure 3, much denser grids with much finer laser lines were used to 'tag' the phosphorescent triplex molecules in the measurement window in order to improve the spatial resolution of the measurements. As described above, the instantaneous velocity distribution can be constructed from the phosphorescence image pair by determining the displacement vectors of the 'tagged' grids between the two interrogations. In the present study, a spatial correlation technique with interrogation window size of 32×32 pixels (~ 1.7 mm $\times$ 1.7 mm in physical space) was used for the image processing to extract flow velocity vectors. The shadow regions of the test cylinder at the upper right corner of the images were blocked during the image processing. Figure 9(*c*) shows the resultant instantaneous velocity distribution with 50 % overlap of the interrogation windows. The alternate shedding of wake vortices at the two sides of the cylinder were revealed clearly in the time sequence of the instantaneous flow velocity distributions, which is a typical behaviour of the wake flow behind an unheated cylinder at a Reynolds number of 135. Based on 360 frames of instantaneous MTV&T measurements, taken at the frame rate of 3.0 Hz, the ensemble-averaged velocity distribution in the cylinder wake was calculated, and the result is shown in figure 9(*d*). A recirculation zone right behind the cylinder can be seen clearly in the ensemble-averaged velocity distribution. The centre of the circulation zone with maximum upward flow velocity was found to be at a downstream location of $X/D \approx 2.0$.

Figures 10(*a*) and 10(*b*) show a typical phosphorescence image pair for the MTV&T measurements when the cartridge heater was turned on. The temperature of the heated cylinder was set to 35.0 °C, corresponding to a Richardson number of 0.19 (i.e. case 2). The resultant velocity vectors derived from the image pair are shown in figure 10(*c*). The instantaneous velocity fields revealed a similar wake vortex shedding process and 'Kármán' vortex street formation as in the wake of the unheated cylinder (i.e. case 1).

In the phosphorescence images shown in figures 10(*a*) and 10(*b*), well-defined thermally induced flow structures in the form of 'dark clusters' can be identified in the wake behind the heated cylinder. The 'dark clusters' are actually the warm fluid shedding periodically from the boundary layer around the heated cylinder. As
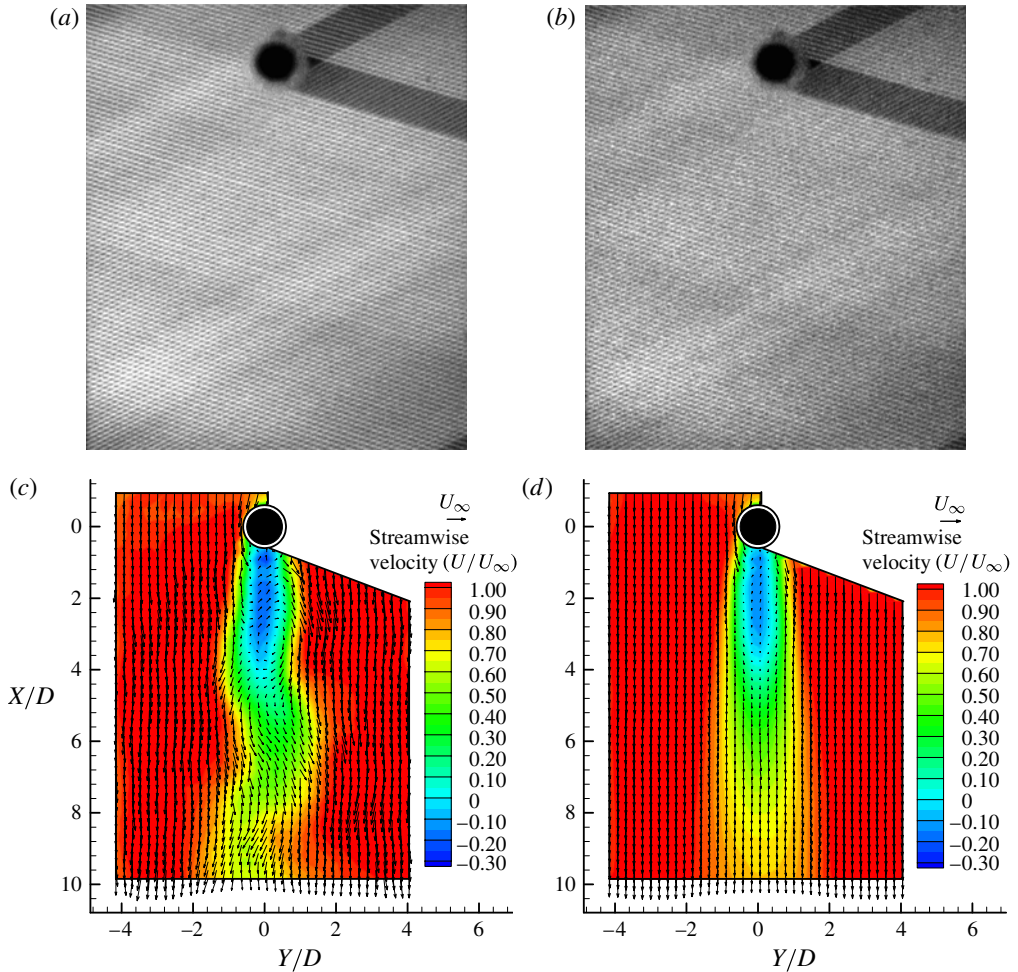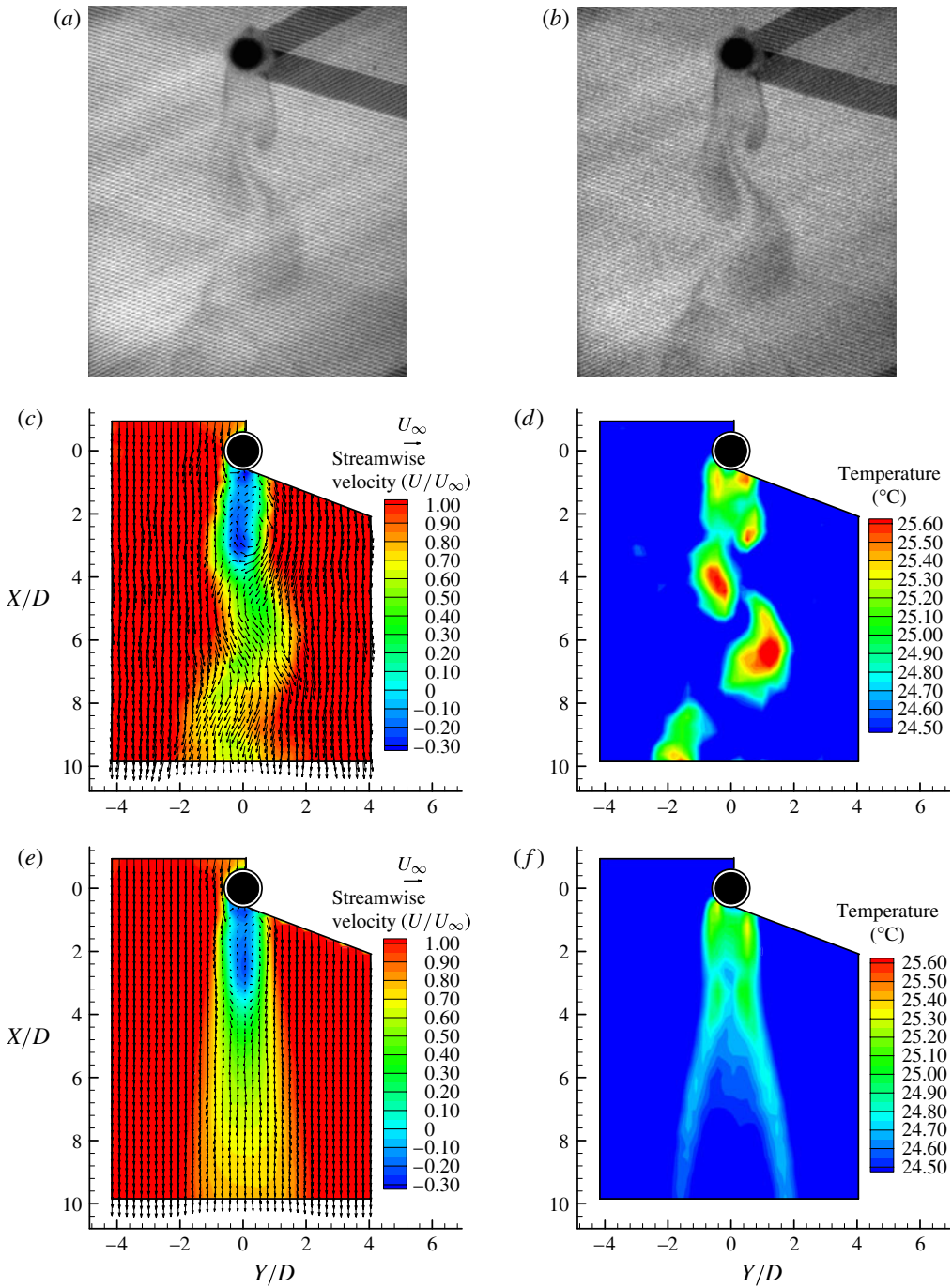
FIGURE 10. MTV&T measurement results for case 2 ($Ri = 0.19$): (*a*) first image (1 ms after laser pulse); (*b*) second image (6 ms after laser pulse); (*c*) instantaneous velocity field; (*d*) simultaneous temperature field; (*e*) averaged velocity (U, V); (*f*) averaged temperature (T).

determine the displacement of the tagged regions, the same interrogation regions with 32×32 pixels in size were chosen in the first phosphorescence image to calculate the averaged phosphorescence intensity S_1 within the regions. The molecules tagged within each region would convect to a new region in the second phosphorescence image according to their Lagrangian displacements over the time interval between the two image acquisitions. The displacement field is, of course, the basis for the flow velocity measurement and already available as shown in figure 10(*c*). The mass diffusion of the tagged molecules out of the interrogation windows is negligibly small, since the mass diffusion length in the present experimental study is $\sim 1/500$ of the interrogation window size. Therefore, for each interrogation window in the first phosphorescence image, the position of the corresponding 'displaced' window in the second phosphorescence image was determined based on the measured flow velocity field in order to calculate the corresponding averaged phosphorescence intensity S_2 within each region. It should be noted that the procedure used here is a first-order method that uses a linear displacement model consistent with the small Lagrangian displacements (i.e. the small time delay between image pair) and relatively small distortion of the tagged regions due to the velocity gradients. Once the averaged phosphorescence intensities, S_1 and S_2, were determined for the corresponding regions in the phosphorescence image pair, the phosphorescence lifetime was calculated based on (2.3), resulting in the measurement of fluid temperature according to the lifetime versus temperature calibration curve shown in figure 6. The derived temperature would represent the spatially averaged temperature over the interrogation window. As described in Hu & Koochesfahani (2006), the averaging of the phosphorescence intensity within each interrogation window is helpful to improve the temperature measurement accuracy, but at the expense of reducing the spatial resolution of the measurements.

The simultaneous temperature field derived from the phosphorescence image pair, which is shown in figure 10(*d*), illustrates the fluid temperature distribution in the wake of the heated cylinder for case 2 ($Ri = 0.19$). The alternate shedding of 'warm blobs' (i.e. fluid with higher temperature) associated with the 'Kármán' vortices can be seen clearly. Similar to the velocity results, the fixed 32×32 pixels (1.7 mm $\times$ 1.7 mm or $0.35D \times 0.35D$ in space) interrogation window size is too large to resolve the details of the initial thermal shear layers that separate from the heated cylinder. The dark regions revealed in the phosphorescence images highlighting the warm boundary layers that separate from the cylinder surface suggest a value of $\sim 0.1D$ for the initial thickness of these thermal shear layers. The temperatures indicated in figure 10(*d*) in those regions are, therefore, highly averaged in spaces and underestimated in magnitude. The measurements become more reliable once the scales of the flow structures become comparable to the cylinder diameter after the shear layers roll up, i.e. in the downstream region of $X/D > 2.5$. The peak temperature in the centre of the 'warm blob' at $X/D \approx 4.5$ and $X/D \approx 6.5$ was found to be $\sim 26.5\,^{\circ}\text{C}$, or a maximum instantaneous temperature differential of $(T_{max} - T_{\infty}) \approx 2.5\,^{\circ}\text{C}$ in the wake behind the heated cylinder for case 2 ($Ri = 0.19$). It should be noted that thermal structures with such small temperature differences could still be revealed with great detail in the MTV&T measurements owing to the high temperature sensitivity of the phosphorescent triplex.

The ensemble-averaged velocity and temperature distributions were calculated based on 360 frames of instantaneous MTV&T measurements, and the results are shown in figures 10(*e*) and 10(*f*). A recirculation zone behind the heated cylinder is revealed clearly in the ensemble-averaged velocity distribution, which is similar to that found

in the wake of the unheated cylinder (figure 9*d*). The recirculation zone for this case is found to become slightly smaller compared with that in the wake of the unheated cylinder (further quantitative comparison will be given later). The ensemble-averaged temperature distribution reveals that two high-temperature regions exist at the two sides of the wake region, corresponding to the shedding paths of the 'Kármán' vortices and the 'warm blobs' revealed in the instantaneous measurement results.

Figure 11 shows a typical pair of phosphorescence images and the corresponding MTV&T measurement results in the wake of the heated cylinder for case 3, where the temperature of the cylinder was increased to 42 °C (i.e. $T_w = 42.0$ °C), corresponding to a Richardson number of 0.31. The instantaneous velocity field revealed a shedding process of the wake vortices to form a 'Kármán' vortex street in the wake behind the heated cylinder similar to that in the wake of the unheated cylinder (i.e. case 1). Compared with case 2, the 'dark clusters' are much more pronounced in the phosphorescence images owing to the higher temperature of the heated cylinder for this case. The instantaneous temperature distribution derived from the phosphorescence image pair elucidates the alternate shedding of the warmer fluid from the boundary layer around the heated cylinder to form 'warm blobs' periodically at two sides of the heated cylinder. The length of the recirculation zone in the ensemble-averaged velocity distribution was found to be almost the same as that in the wake of the unheated cylinder (i.e. case 1), and slightly longer compared with that of case 2. While similar temperature distribution patterns can be seen in the averaged temperature distributions for cases 2 and 3, a slightly higher temperature was found in the wake of the heated cylinder for case 3 because of the higher wall temperature of the cylinder in that case.

Figure 12 shows a typical pair of phosphorescence images and the resulting velocity and temperature distributions in the wake of the heated cylinder for case 4, where the temperature of the heated cylinder was increased to 53 °C, corresponding to a Richardson number of 0.50. Compared with previous cases with smaller Richardson number, the shedding process of the 'Kármán' vortices and 'warm blobs' for this case was found to show the first evidence for significant change due to the stronger thermal effects. Although the shedding process of vortices was still noted to occur alternately at two sides of the heated cylinder, the periodic shedding was 'delayed', taking place much further downstream compared with the cases with smaller Richardson numbers. The appearance of the first 'Kármán' vortex and 'warm blob' was found to be at ∼6 cylinder diameters downstream of the heated cylinder (i.e. $X/D \approx 6.0$), while it was ∼2 ∼ 3 cylinder diameters downstream for the cases with smaller Richardson number (i.e. cases 2 and 3). The instantaneous temperature field revealed that the warm boundary layers that separate from the heated cylinder surface had become much thicker for this case with a higher Richardson number.

The ensemble-averaged velocity and temperature distributions revealed that the wake flow pattern downstream of the heated cylinder became significantly different from those previous cases with smaller Richardson numbers. Instead of having a strong recirculation zone right downstream of the cylinder, a long 'dead flow' zone with nearly zero velocity was found to be located in the near wake with an extent reaching as far as $X/D \leqslant 3.5$. A larger and stronger recirculation zone was found to exist, but further downstream, and its centre with maximum upward velocity was located at the downstream location $X/D \approx 6.0$. Significant differences also appeared in the mean temperature distribution when compared to cases with smaller Richardson numbers. The thermal wake (i.e. the regions with higher temperature) behind the heated cylinder was found to become much wider. The maximum instantaneous temperature difference in the wake grew larger to ∼4.5 °C for this case.

FIGURE 11. MTV&T measurement results for case 3 ($Ri = 0.31$): (*a*) first image (1 ms after laser pulse); (*b*) second image (6 ms after laser pulse); (*c*) instantaneous velocity field; (*d*) simultaneous temperature field; (*e*) averaged velocity (U, V); (*f*) averaged temperature (T).
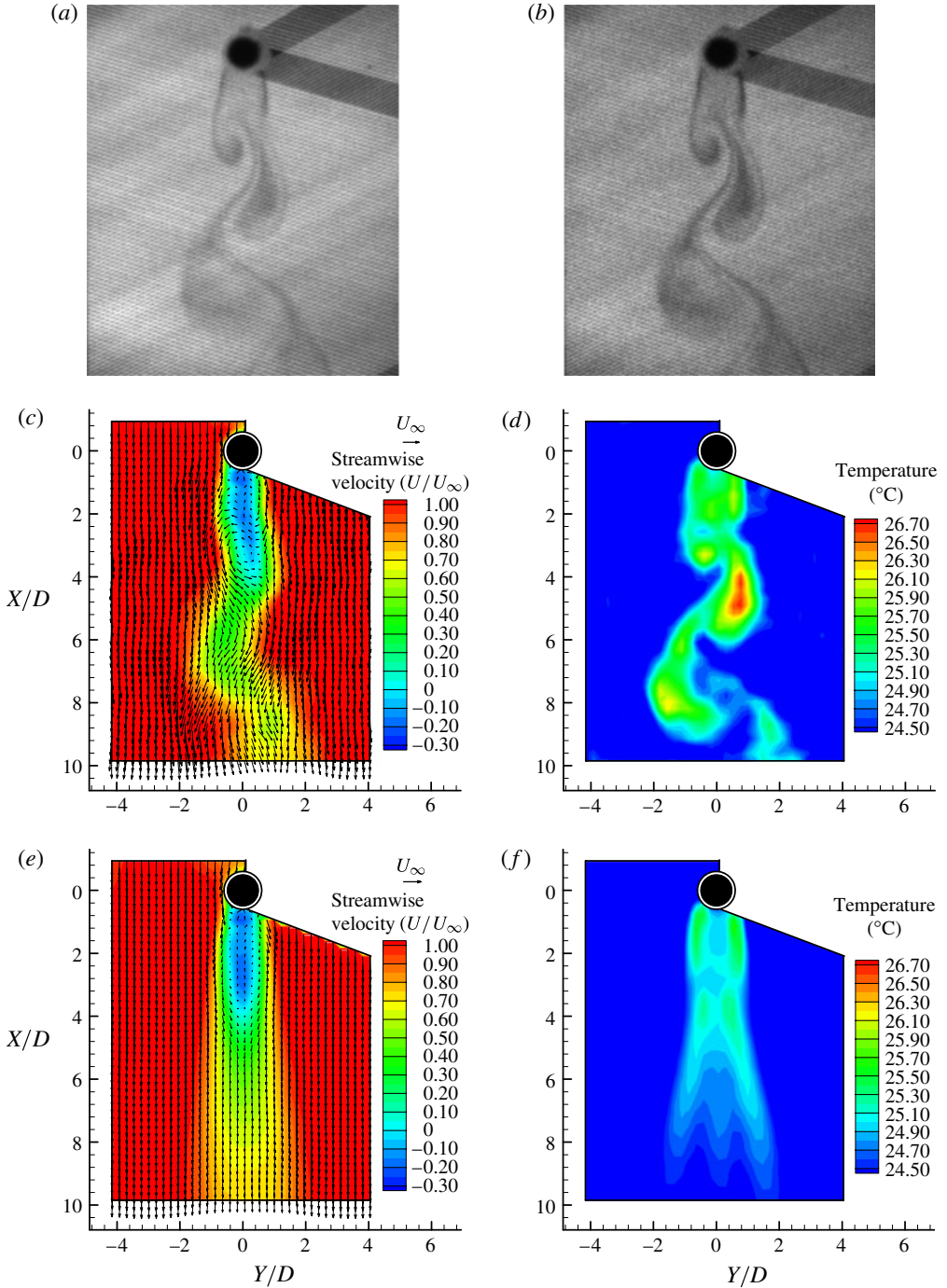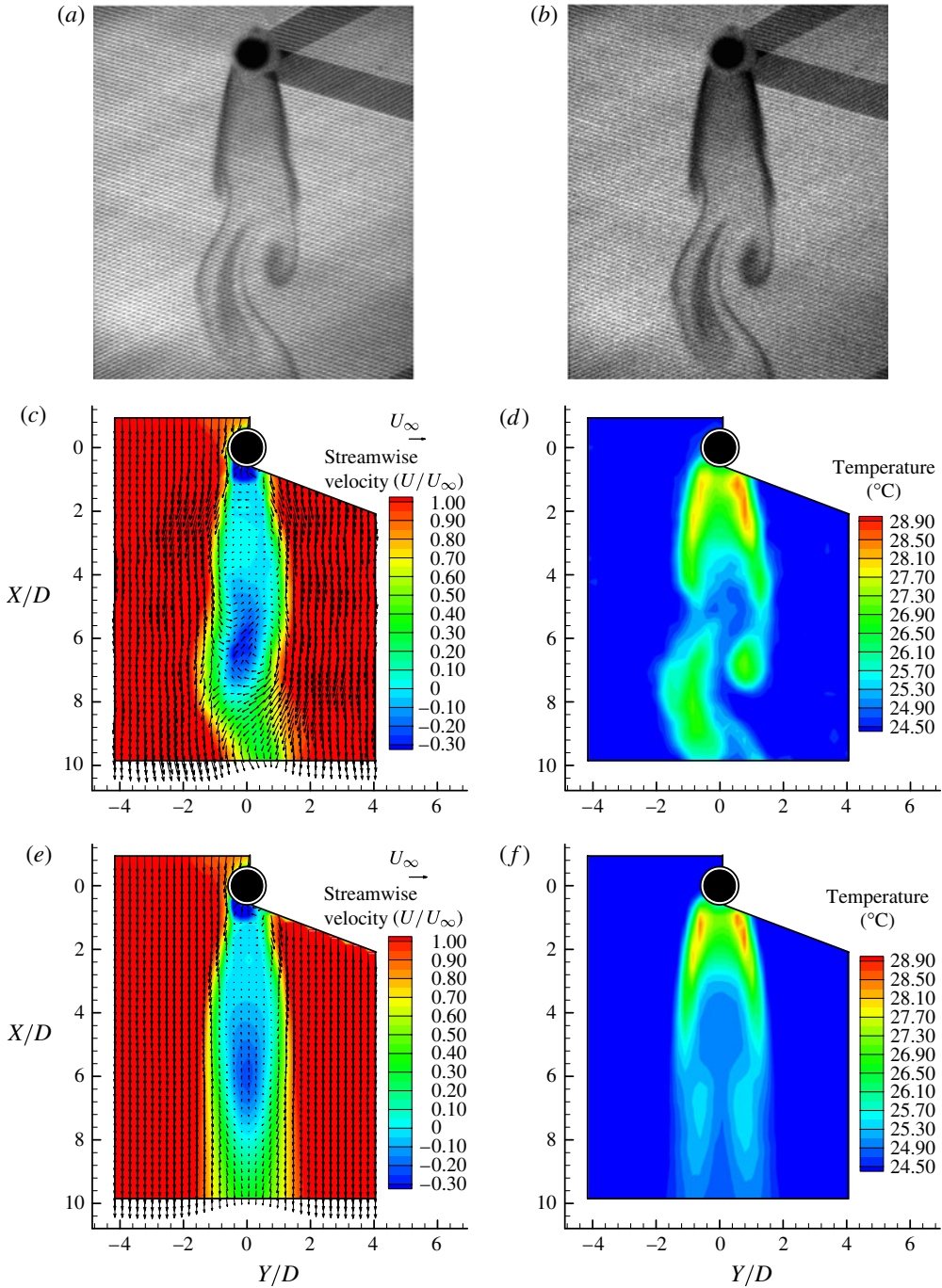
FIGURE 12. MTV&T measurement results for case 4 ($Ri = 0.50$): (*a*) first image (1 ms after laser pulse); (*b*) second image (6 ms after laser pulse); (*c*) instantaneous velocity field; (*d*) simultaneous temperature field; (*e*) averaged velocity (U, V); (*f*) averaged temperature (T).

A representative phosphorescence image pair and resultant MTV&T measurement results are shown in figure 13 for case 5, where the temperature of the heated cylinder was increased to 66 °C, with the corresponding Richardson number of 0.72. The vortex shedding process in the wake was found to become completely different in this case compared to all previous cases. Instead of a pattern of alternate shedding of the 'Kármán' vortices, the vortex structures and 'warm blobs' were found to shed almost concurrently at the two sides of the heated cylinder, and their sizes were slightly smaller than those at smaller Richardson numbers. Compared with case 4 ($Ri = 0.5$), the 'dead flow' zone in the wake was observed to become longer and wider. The large recirculation zone further downstream was also found to become longer and wider, with the centre of the recirculation zone moving further downstream to $X/D \approx 7.0$. The mean temperature distribution revealed a region with high temperature near the rear end of the heated cylinder. The maximum instantaneous temperature difference in the wake flow was found to be ~ 5.5 °C for this case.

As the temperature of the heated cylinder increased to $T_w = 85.0$ °C (i.e. case 6, with Richardson number of 1.04), the concurrent shedding of smaller vortex structures or 'warm blobs' at two sides of the heated cylinder could be seen more clearly from the phosphorescence images and the MTV&T measurement results shown in figure 14. These smaller wake vortex structures were noted to behave more like 'Kelvin–Helmholtz' structures than 'Kármán' wake vortex structures. Inspection of the time sequences of the instantaneous MTV&T measurement results revealed that adjacent small vortex structures at each side of the heated cylinder would merge to form larger vortex structures or larger 'warm blobs' in the region $5.0 \leqslant X/D \leqslant 7.0$. The merging process was found to be similar to the 'pairing' process of 'Kelvin–Helmholtz' vortex structures in a free shear layer. The merging of the smaller vortices was observed to occur alternately at two sides of the wake, which led to the final alternate shedding of larger 'Kármán' vortex structures and 'warm blobs' further downstream. The ensemble-averaged velocity field reveals that the wake region behind the heated cylinder became even longer and wider at this high Richardson number ($Ri = 1.04$). The strong recirculation zone downstream of the cylinder became very long and extended up to 10 diameters downstream. The longer and wider wake region could also be seen clearly from the mean temperature distribution, with the maximum instantaneous temperature difference in the wake reaching ~ 6.0 °C in this case.

4.2. *Heat flux measurements*

Quantitative information about the turbulent heat flux, which is the correlation between the unsteady flow velocity and fluid temperature, would be very helpful to gain insight into the convective heat transfer process from a heated cylinder to ambient flow and to elucidate the underlying physics. However, measurement of the turbulent heat flux distribution in a thermal fluid flow is technically quite challenging, since it requires quantitative measurements of the unsteady flow velocity and temperature fields at the same time. The work of Park, Dabiri & Gharib (2001) is among the very few that has ever reported measurements of the turbulent heat flux distribution in the wake of a heated cylinder using the digital particle velocimetry and thermometry (DPIV/T) technique.

Since the MTV&T technique used in the present study is capable of measuring unsteady flow velocity and temperature fields simultaneously, the turbulent heat flux distribution in the wake of the heated cylinder can be easily determined. As demonstrated in Park *et al.* (2001), the overall global turbulent heat flux in the

FIGURE 13. MTV&T measurement results for case 5 ($Ri = 0.72$): (*a*) first image (1 ms after laser pulse); (*b*) second image (6 ms after laser pulse); (*c*) instantaneous velocity field; (*d*) simultaneous temperature field; (*e*) averaged velocity (U, V); (*f*) averaged temperature (T).
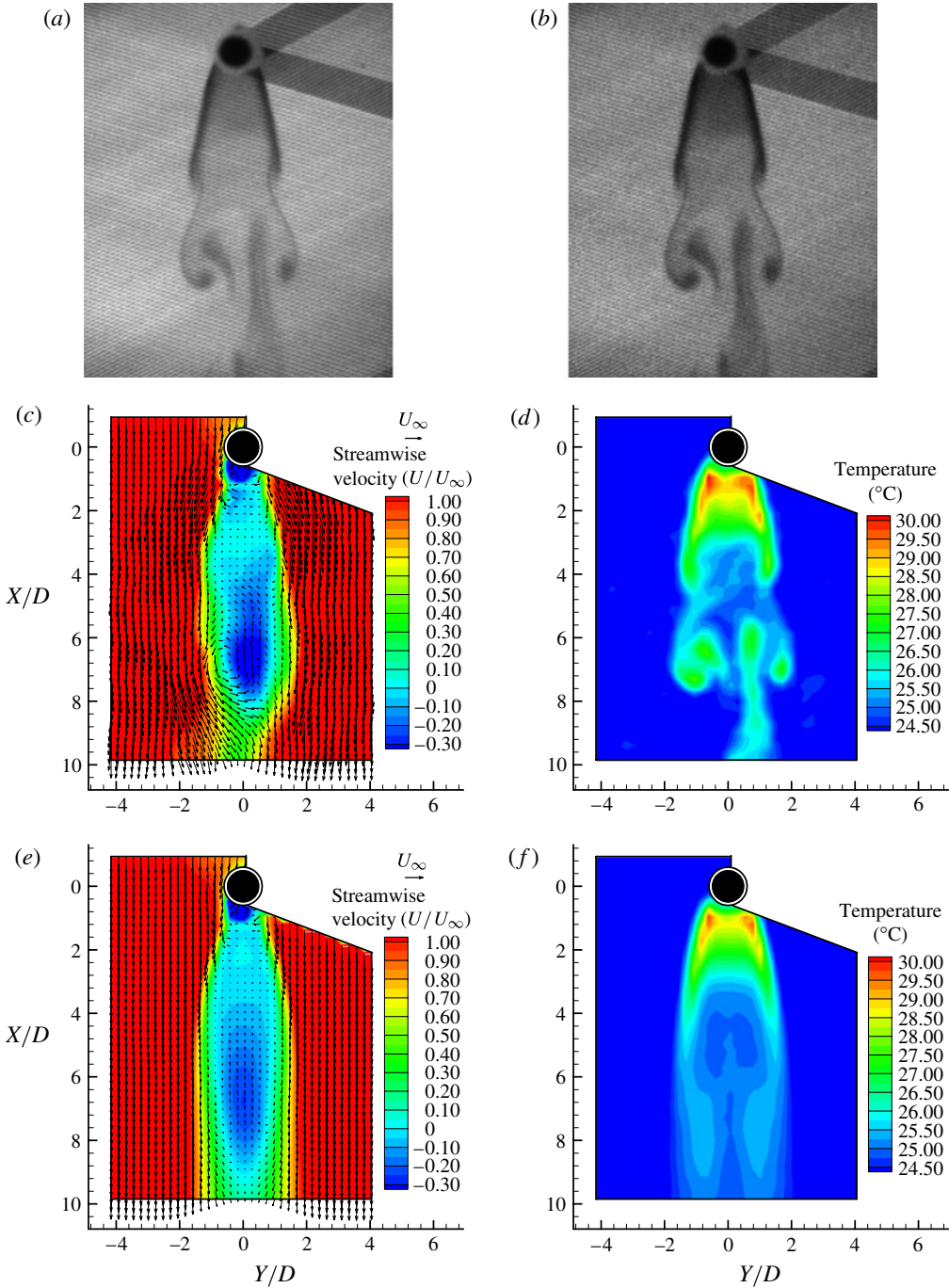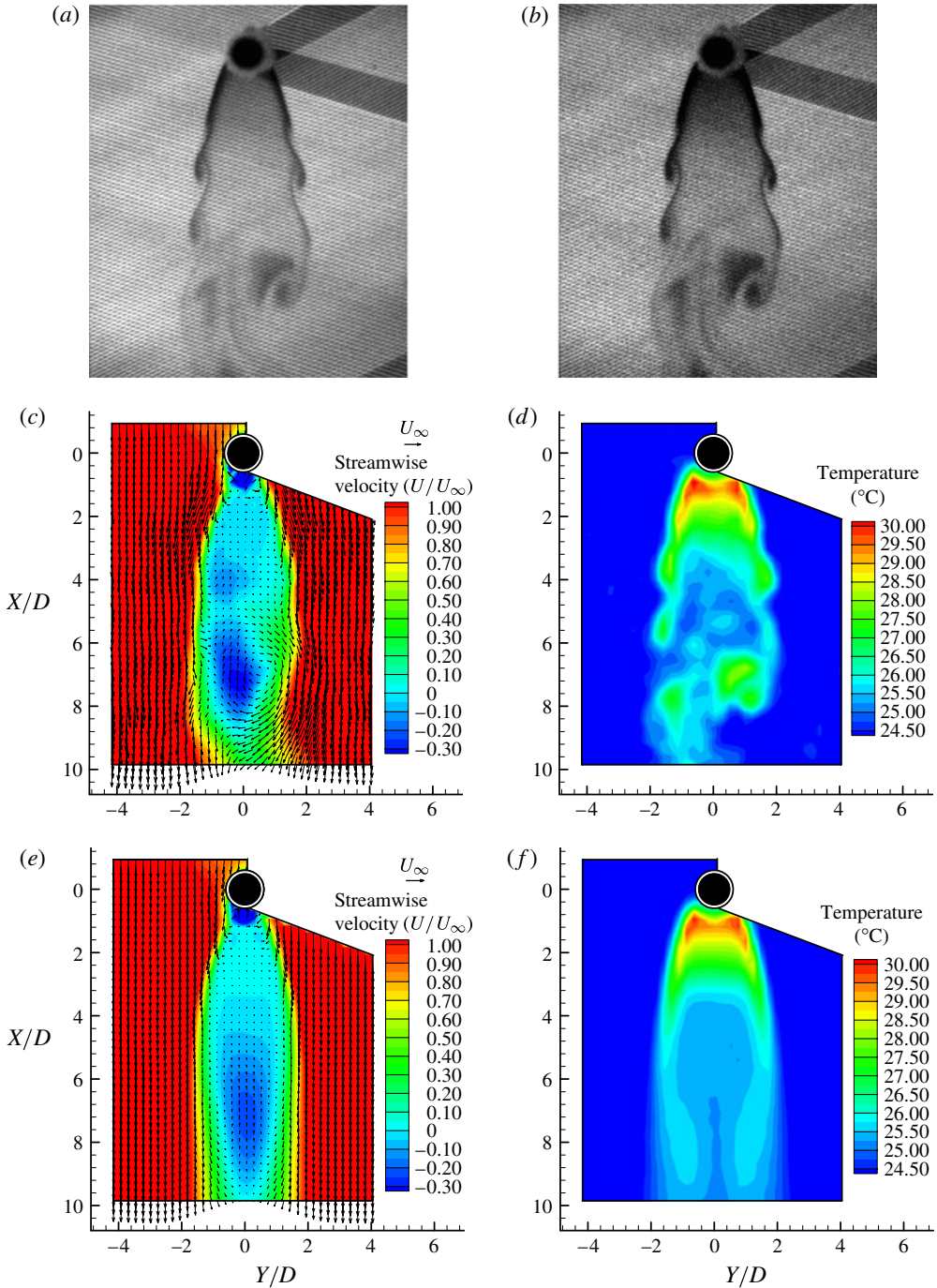
FIGURE 14. MTV&T measurement results for case 6 ($Ri = 1.04$): (*a*) first image (1 ms after laser pulse); (*b*) second image (6 ms after laser pulse); (*c*) instantaneous velocity field; (*d*) simultaneous temperature field; (*e*) averaged velocity (U, V); (*f*) averaged temperature (T).

wake of the heated cylinder may be decomposed into the mean, periodic and incoherent components. In the present study, however, we report only the results for the global turbulent heat flux. The global turbulent heat flux vector $(\overline{u'T'}, \overline{v'T'})$ was calculated based on the 360 instantaneous realizations (i.e. $N = 360$) from MTV&T measurements using the usual expressions for velocity–temperature correlation, which are given below for completion:

$$\left.\begin{aligned}
\overline{u'T'} &= \frac{1}{N} \sum_{t=1}^{t=360} \left(\frac{u(t)}{U_\infty} - \frac{U}{U_\infty} \right) \left(\frac{T(t)}{T_\infty} - \frac{\overline{T}}{T_\infty} \right), \\
\overline{v'T'} &= \frac{1}{N} \sum_{t=1}^{t=360} \left(\frac{v(t)}{U_\infty} - \frac{V}{U_\infty} \right) \left(\frac{T(t)}{T_\infty} - \frac{\overline{T}}{T_\infty} \right), \\
U &= \frac{1}{N} \sum_{t=1}^{t=360} u(t), \quad V = \frac{1}{N} \sum_{t=1}^{t=360} v(t), \quad \overline{T} = \frac{1}{N} \sum_{t=1}^{t=360} T(t).
\end{aligned}\right\} \tag{4.1}$$

The spatial map of the measured global turbulent heat flux vectors is illustrated in figure 15, where the magnitude of the turbulent heat flux vector, defined as $\mathrm{THF} = \sqrt{(\overline{u'T'})^2 + (\overline{v'T'})^2}$, is also shown as a colour contour map in the background. In interpreting this figure, it is important to recognize that, as described earlier, the small vortex structures and the thin thermal boundary layer around the heated cylinder could not be well resolved in the current measurements owing to spatial resolution limitations. Therefore, no apparent flow structures could be identified in the measured turbulent heat flux fields in the near region of $X/D < 2.5$ in any of the cases studied. The instantaneous velocity and temperature distributions, discussed previously, indicated that the wake vortices and thermal structures would be resolved well in the MTV&T measurements when their size grew to be comparable to the cylinder diameter further downstream in the region $X/D > 2.5$. As a result, in this region vortex-like structures can be identified clearly in measured turbulent heat flux fields shown in figure 15.

The thermally induced effects on the convective heat transfer process in the wake of the heated cylinder is revealed clearly from the comparison of the measured heat flux vector distributions at different Richardson numbers in figure 15. While the magnitude of the measured heat flux vectors can be used to indicate how fast the heat convection process will be, the direction of the heat flux vectors would quantitatively visualize the direction along which the convective heat transfer process will be conducted in the wake of the heated cylinder. As shown in figure 15, the structure of measured turbulent heat flux $(\overline{u'T'}, \overline{v'T'})$ in the wake is dominated by two large counter-rotating vortex-like structures, which are almost symmetrical about the wake centreline. As the Richardson number increases, these structures were found to grow and move further downstream, corresponding to the 'delayed' appearances of the 'Kármán' vortex structures and 'warm blobs' revealed in the instantaneous velocity and temperature measurement results described previously. The counter-rotating vortex-like structures in the measured turbulent heat flux vector fields are believed to be closely related to the entrainment of the cold free-stream fluid by the shedding of 'Kármán' vortices in the wake behind the heated cylinder. Similar structures were also reported by Park *et al.* (2001) in their measurements of the turbulent heat flux in the wake of a heated cylinder using the DPIV/T technique.
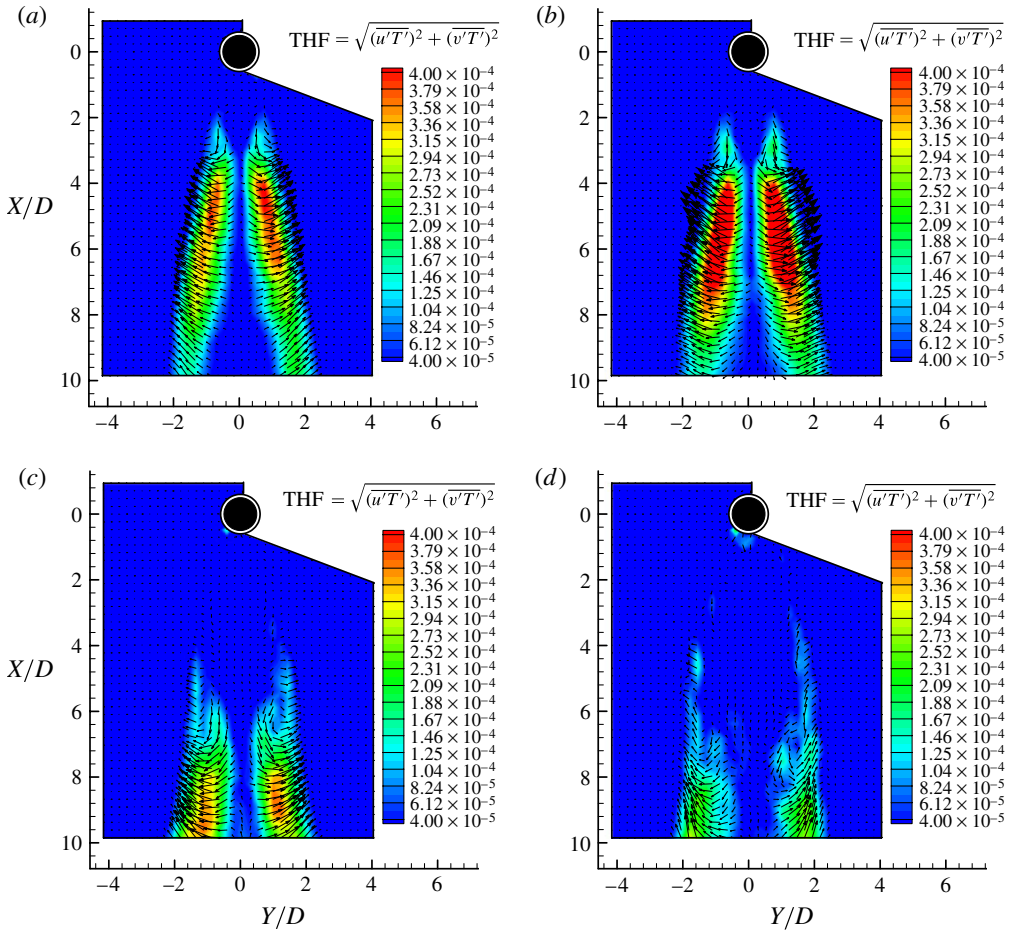
FIGURE 15. Measured turbulent heat flux vectors in the wake of the heated cylinder:
(*a*) $Ri = 0.19$; (*b*) $Ri = 0.31$; (*c*) $Ri = 0.50$; (*d*) $Ri = 1.04$.

4.3. *Velocity variation along the wake centreline*

The discussion in §4.1 pointed to the significant changes that occurred in the wake
of the heated cylinder in terms of the flow pattern and the temperature field. In this
section we focus more closely on the thermal effects on the recirculation region in the
near wake and the wake closure length.

In figure 16 the variation of the ensemble-averaged streamwise velocity profiles
along the wake centreline is displayed as a function of downstream distance for
different Richardson numbers. The results given in figure 16 clearly show that the
wake centreline velocity variation in the wake of the heated cylinder can be divided
into two groups: one group is for the cases with relatively small Richardson number
($Ri \leqslant 0.31$); and the other is for the cases with relatively large Richardson number
($Ri \geqslant 0.50$). When the Richardson number was relatively small ($Ri \leqslant 0.31$), the
streamwise velocity profiles along the wake centreline were noted to be very similar
to the unheated cylinder case (i.e. $Ri = 0.0$). This was characterized by negative
streamwise velocities in the region of $X/D < 3.5$, consistent with the existence of a
recirculation zone behind the cylinder as revealed in the ensemble-averaged velocity
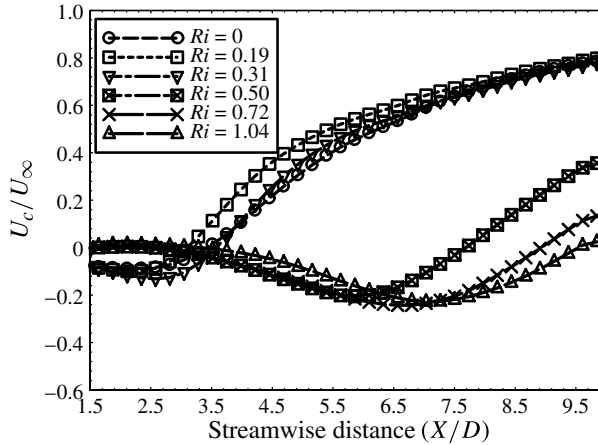
FIGURE 16. Streamwise velocity profiles along the wake centreline.

distributions. These negative velocities were found to recover (i.e. increase to become positive) gradually as the downstream distance increases.

For the unheated case (i.e. $Ri = 0.0$), the wake centreline velocity was found to change its sign and become positive at $X/D \approx 3.5$. Compared with the unheated cylinder, the recovery of the centreline velocity for case 2 ($Ri = 0.19$) was slightly faster, and the wake centreline velocity was found to become positive at the downstream location of $X/D \approx 3.0$, indicating a shorter recirculation zone, as also shown in the ensemble-averaged velocity distribution in figure 10. For case 3 ($Ri = 0.31$), the recovery characteristics of the streamwise velocity along the wake centreline became almost the same as that of the unheated cylinder, with the change from negative to positive velocity occurring at the downstream location $X/D \approx 3.5$.

As the Richardson number became relatively large ($Ri \geqslant 0.50$), the profiles of the streamwise velocity along the wake centreline were found to become significantly different from those with relatively small Richardson numbers ($Ri \leqslant 0.31$). Consistent with the ensemble-averaged velocity distributions described earlier, a 'dead flow' zone, with near zero flow velocity, was discovered in the near wake region for Richardson numbers $Ri \geqslant 0.50$. According to figure 16, for these cases the wake centreline velocity stayed flat near the zero value in the downstream region $X/D \leqslant 3.5$. Beyond this region, the wake centreline velocity gradually became negative (i.e. upward streamwise velocity) until reaching their upward velocity peaks (i.e. the centres of the recirculation zones). The recirculation zone with strong upward (negative) flow velocity was, therefore, pushed further away from the heated cylinder. Ultimately, these negative velocities would recover slowly and become positive with increasing distance away from the heated cylinder, but much further downstream compared to the cases at the lower range of Richardson numbers.

Using the data in figure 16, we can determine the wake closure length (l_C), defined as the distance behind the cylinder where the centreline velocity goes through zero as it changes its sign from negative to positive. Figure 17 depicts the measured wake closure length (l_C) as a function of Richardson number for the present study. For the unheated cylinder ($Ri = 0.0$), the wake closure length was found to be ∼3 cylinder diameters. This result is consistent with that reported by Michaux-Leblond & Belorgey (1997) for an unheated cylinder at $Re = 130$. For the relatively small Richardson
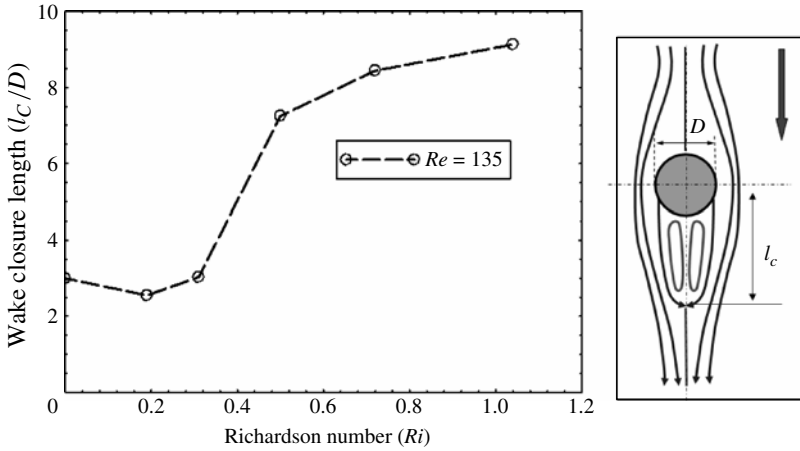
FIGURE 17. Wake closure length (l_C) versus Richardson number (Ri).

number of $Ri \approx 0.19$, the wake closure length decreased to $\sim l_C/D \approx 2.5$, slightly shorter than that of the unheated cylinder. As the Richardson number increased to 0.31, the wake closure length was found to have increased again to $l_C/D \approx 3.0$, almost the same as the unheated cylinder case. When the Richardson number became relatively large (i.e. $Ri > 0.50$), the wake closure lengths were found to increase rapidly. At the largest Richardson number in our study, $Ri = 1.04$, the wake closure length had reached a value as high as $l_C/D \approx 9$.

The equivalence of thermally induced effects to a corresponding streamwise pressure gradient over the surface of the heated cylinder may be used to explain qualitatively certain aspects of the experimental observation described above. Referring to the schematic of coordinates in figure 18, the thermal boundary-layer equation for steady two-dimensional flow can be written as (see Schlichting 1979)

$$\rho_\infty \left(u \frac{\partial u}{\partial x} + v \frac{\partial u}{\partial y} \right) = -\frac{\mathrm{d}p}{\mathrm{d}x} + \frac{\partial}{\partial y} \left(\mu \frac{\partial u}{\partial y} \right) - \rho_\infty g \beta (T - T_\infty) \cos \alpha, \qquad (4.2)$$

where β is the thermal expansion coefficient. Evaluating this equation at the surface of the cylinder where $(u = 0, v = 0)$, and taking into account the variable viscosity due to non-uniform temperature, leads to

$$0 = -\frac{\mathrm{d}p}{\mathrm{d}x} + \left. \frac{\partial \mu}{\partial y} \right|_w \left. \frac{\partial u}{\partial y} \right|_w + \mu_w \left. \frac{\partial^2 u}{\partial y^2} \right|_w - \rho_\infty g \beta (T_w - T_\infty) \cos \alpha, \qquad (4.3)$$

where subscript w represents wall quantities at the cylinder surface. Using free-stream conditions $(U_\infty, T_\infty, \rho_\infty, \mu_\infty)$ and cylinder diameter D as reference variables, and solving for the velocity profile curvature at the wall, results in the following final non-dimensional form:

$$\frac{1}{Re} \left(\mu_w^* \left. \frac{\partial^2 u^*}{\partial y^{*2}} \right|_w \right) = \frac{\mathrm{d}p^*}{\mathrm{d}x^*} - \underbrace{\frac{1}{Re} \left. \frac{\partial \mu^*}{\partial y^*} \right|_w \left. \frac{\partial u^*}{\partial y^*} \right|_w}_{\text{I}} + \underbrace{\frac{Gr}{Re^2} \cos \alpha}_{\text{II}} . \qquad (4.4)$$

The connection between the velocity profile curvature at the wall and the imposed pressure gradient is commonly used in isothermal flows (where both terms I and II
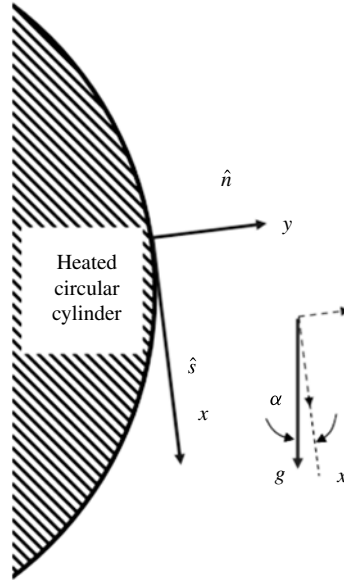
FIGURE 18. Schematic used for modelling the thermal effects on the streamwise pressure gradient over the surface of a heated cylinder.

are zero) to describe the influence of favourable (adverse) pressure gradient in delaying (promoting) flow separation. We note that for a heated wall two new effects appear: term I accounts for the influence of variable viscosity caused by wall heating; and term II represents thermally induced buoyancy. In the current work with water as the working fluid, term I is positive for a heated wall and its effect is equivalent to an imposed favourable pressure gradient ($dp/dx < 0$), whereas term II, which is also positive, has the opposite effect and is equivalent to an adverse pressure gradient ($dp/dx > 0$). Note that term II is essentially the Richardson number ($Ri = Gr/Re^2$) in the area over the cylinder surface where flow separation might be expected to occur (i.e. $\cos \alpha$ is close to unity).

According to (4.4), when the heated cylinder Richardson number is small, thermally induced buoyancy effects represented by term II are expected to be negligible. However, term I imposes an equivalent weak favourable pressure gradient, which leads to delayed flow separation from locations further downstream. This results in a slightly shorter recirculation length, as supported by the experimental results already discussed. As the Richardson number increases, buoyancy effects given by term II start to become dominant, imposing an equivalent adverse pressure gradient. This moves the separation point further upstream, resulting in a wider wake and longer recirculation zone. The larger the Richardson number, the larger the equivalent adverse pressure gradient, and the larger the size of the wake. These qualitative expectations are consistent with the experimental results presented earlier.

4.4. *The Strouhal number of the wake vortex shedding*

Based on the time sequences of the instantaneous MTV&T measurements, the shedding frequency f of the vortex structures in the wake of the cylinder and the corresponding Strouhal number, $St = fD/U_\infty$, can be determined. The Strouhal numbers given in figure 19 were determined from the time series of the measured
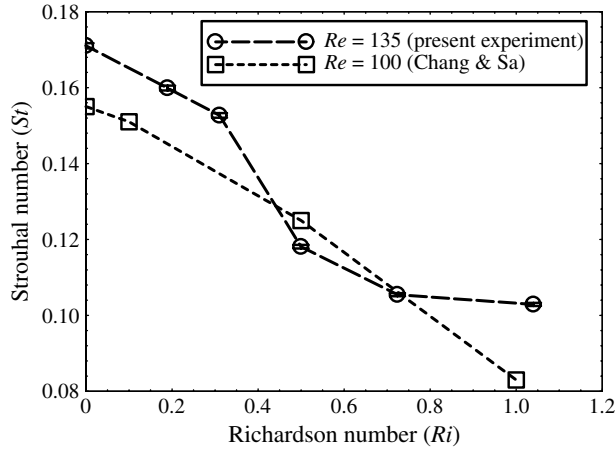
FIGURE 19. Strouhal number versus Richardson number.

velocity at the downstream location of $(X/D = 8.0, Y/D = 1.25)$. The measurement uncertainty due to the limited sample size (360 frames) is also given in the figure as the error bars (at this scale entirely within the size of the circles). It was described earlier that for $Ri \geqslant 0.72$ small vortices initially formed on the two sides of the wake, which then merged in the region $5.0 \leqslant X/D \leqslant 7.0$ to form the larger 'Kármán' vortex structures. The selected measurement location $(X/D = 8.0)$ was sufficiently downstream to capture the shedding frequency of the large 'Kármán' wake vortices.

As shown in figure 19, the present study revealed that the Strouhal number of the wake vortex shedding would decrease monotonically with increasing Richardson number. The measured Strouhal number for the unheated case $(Ri = 0.0)$ was found to be $St = 0.171$. A universal Strouhal–Reynolds number relationship for vortex shedding from a circular cylinder in isothermal flow, proposed by Williamson (1988), is expressed as

$$St = \frac{A}{Re} + B + C\,Re, \tag{4.5}$$

where $A = -3.3265$, $B = 0.1816$ and $C = 1.6 \times 10^{-4}$. The formula has been tested as a good representation in the Reynolds number range $49 < Re < 178$. For the current experiments at $Re = 135$, this formula predicts a shedding Strouhal number of 0.178, which agrees with the measured results to within 4 %.

Figure 19 also compares the current results (in contra-flow with heated cylinder in a vertically downward flow) with the numerical simulation results of Chang & Sa (1990) for a cooled cylinder in an upward forced flow (i.e. contra-flow arrangement) at the Reynolds number of $Re = 100$. It can be seen that both the present experimental study and the numerical simulation of Chang & Sa (1990) reveal a similar decreasing trend for the Strouhal number of vortex shedding with increasing Richardson number. However, some differences exist as well. The results of Chang & Sa (1990) show the Strouhal decreasing almost linearly with increasing Richardson number. Our measurements display a linear decrease only initially, when the Richardson number was relatively small $(Ri \leqslant 0.31)$. The Strouhal number was found to decrease very rapidly when the Richardson number increased from 0.31 to 0.50, and then the rate of decrease became much more moderate beyond the

Richardson number of 0.72. Our Strouhal number data exhibit the same two distinct regions in behaviour for small ($Ri \leqslant 0.31$) and large ($Ri \geqslant 0.50$) Richardson numbers that were noted previously in describing other features of the flow. The differences in Strouhal number behaviour between Chang & Sa (1990) and our experimental results are believed to be closely related to the new findings of the present study about the significant changes in the wake flow pattern and wake vortex shedding process that occur at relatively large Richardson numbers. As described before, the vortex shedding process in the wake of the heated cylinder was found to be similar to that of an unheated cylinder when the Richardson number was relatively small ($Ri \leqslant 0.31$). The vortex shedding process was 'delayed', and the appearance of the first wake vortex occurred much further downstream, when the Richardson number increased to $Ri \approx 0.50$. Instead of alternate shedding of 'Kármán' vortices from the two sides of the heated cylinder, concurrent shedding of smaller vortex structures was observed in the wake for Richardson numbers $Ri \geqslant 0.72$. The small vortex structures behaved more like 'Kelvin–Helmholtz' vortices, and adjacent small vortices would merge to form the larger 'Kármán' vortex structures further downstream. Such significant changes in the wake vortex shedding process, with increasing Richardson number, were not found in the numerical simulation of Chang & Sa (1990).

There has not been a commonly accepted formula to predict the vortex shedding Strouhal number in the wake of a heated cylinder. When the Richardson number is very small and the heated cylinder operates in the forced convection regime, thermally induced effects on the wake instabilities can be neglected. However, the temperature differences within the wake flow would lead to variations in fluid properties: viscosity, density and thermal conductivity. Based on the idea that the temperature differences within the thermal boundary layer around the heated cylinder leads to changes in fluid kinematic viscosity, Dumouchel, Lecordier & Paranthoen (1998) and Wang, Travnicek & Chia (2000) suggested the concept of effective Reynolds number based on an effective temperature $T_{eff} = T_\infty + C(T_w - T_\infty)$, where C is an empirical constant, in order to study the effects of heating on vortex shedding frequency behind heated cylinders in air flows. They found that the Strouhal–Reynolds formula used for the prediction of vortex shedding behind an unheated cylinder is still applicable to heated cylinders by adopting the effective Reynolds number concept. More recently, Vít *et al.* (2007) also confirmed that the concept of effective Reynolds number would be applicable for both air and water flows if the heated cylinder operates in the forced convection region. They also suggested that the empirical constant, C, should be 0.97 for water flows, whereas the constant was suggested by Wang *et al.* (2000) to be 0.28 for air flows. It should be emphasized that the studies of Dumouchel *et al.* (1998), Wang *et al.* (2000) and Vít *et al.* (2007) were all in the forced convection regime at very small Richardson numbers.

Even though the effective Reynolds number concept was developed for forced convection, it would be tempting to determine its prediction for the current (mixed convection) studies. Such a prediction would suggest an increase in Strouhal number from 0.178 for the baseline unheated cylinder ($Ri = 0$, $Re = Re_{eff} = 135$) to $\sim$0.23 for the heated cylinder at $Ri = 1.04$ ($Re = 135$, $Re_{eff} = 360$). This trend is completely opposite to our experimental data, where the Strouhal number decreased from 0.171 for the unheated cylinder to 0.106 for the heated cylinder at $Ri = 1.04$. It suggests that the effective Reynolds number approach is not applicable to the prediction of the wake vortex shedding from a heated cylinder operating in the mixed convection regime in contra-flow arrangement.
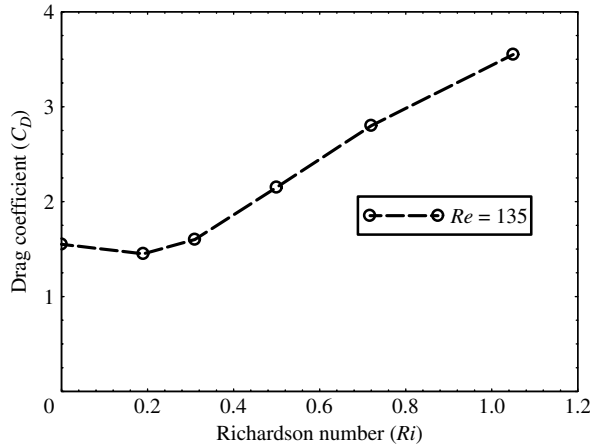
FIGURE 20. Drag coefficient versus Richardson number.

4.5. *Drag coefficient of the heated cylinder*

The measured velocity data were utilized to obtain the drag coefficient of the cylinder and to determine the influence of cylinder heating on the drag force. Using the information given in Bohl & Koochesfahani (2009) based on control volume analysis, the mean drag coefficient was estimated from the following expression:

$$
C_D \approx \frac{2}{D} \int_{-H}^{+H} \left\{ \frac{U(y)}{U_\infty} \left(1 - \frac{U(y)}{U_\infty} \right) - \frac{u_{rms}^2(y) - v_{rms}^2(y)}{U_\infty^2} \right.
$$
$$
\left. + \frac{1}{2} \left(\frac{U_{free\text{-}stream}^2}{U_\infty^2} - 1 \right) \right\} dy. \tag{4.6}
$$

In this expression, U_∞ is the upstream flow velocity, $U(y)$ is the mean streamwise velocity profile in the wake, u_{rms} and v_{rms} are the r.m.s. profiles of the streamwise and transverse velocity fluctuations, and $U_{free\text{-}stream}$ is the free-stream velocity outside the wake region and is higher than U_∞ due to the finite width of the test section. The last term on the right-hand side accounts for the corresponding pressure change in the free stream. The integration domain corresponds to $H/D = 4.0$ and the force calculation was carried out based on the measured profiles at $X/D = 8.0$.

The estimated drag coefficient C_D of the heated cylinder is illustrated in figure 20 for different Richardson numbers. For the unheated cylinder ($Ri = 0.0$), C_D was found to be ~1.5, a value that is consistent with the data given in Schlichting (1979). The data in figure 20 reveal that an increase in the temperature of the heated cylinder initially led to a very slight decrease in drag coefficient (at $Ri = 0.19$), followed by a monotonic increase in C_D with increasing Richardson number. As the Richardson number became large enough ($Ri > 0.31$), the drag coefficient increased almost linearly with Richardson number. At the largest Richardson number of 1.04, the drag coefficient was found to be ~3.5, nearly 2.5 times higher than that for the unheated cylinder.

The total drag force acting on a circular cylinder is the sum of friction drag and pressure drag, with the pressure drag accounting for the bulk of the overall drag at the Reynolds number of the current work. The general trend of drag coefficient

in figure 20 is consistent with the size of the wake recirculation zone discussed earlier in figure 17, with the larger wake implying a larger pressure drag. At the small Richardson number of $Ri = 0.19$, the small reduction in C_D is thought to be the combined effect of the wake recirculation region being slightly smaller than the unheated cylinder (see figure 17), in addition to reduced friction drag due to smaller viscosity at higher temperature. At higher Richardson numbers, the large increase in the size of the recirculation zone is the primary influence that leads to the increased drag force on the heated cylinder.

4.6. *Average Nusselt number* $(\overline{Nu})$

The power dissipated by the heater in the experiments was measured by monitoring the voltage and current supplied to the cartridge heater during the experiments. Considering the power losses through end pieces of the cartridge heater, it was estimated that ~90 % of the total electrical power supplied to the heater was dissipated by the approaching forced flow inside the water channel. The average Nusselt numbers $(\overline{Nu})$ of the heated cylinder at different Richardson numbers were calculated based on the following relation (Incropera & Dewitt 2001):

$$\overline{Nu} = \frac{hD}{k_\infty} = \frac{1}{k_\infty}\frac{q}{A(T_w - T_\infty)}D = \frac{q}{\pi L k_\infty(T_w - T_\infty)}, \qquad (4.7)$$

where the q is the heat flux dissipated by the approaching forced flow, L is the spanwise length of the cartridge heater inside the water channel, k_∞ is the thermal conductivity of the approach flow, and T_w and T_∞ are the temperatures of the heated cylinder and the approach flow, respectively.

For a heated cylinder operating in the forced convection regime, the empirical correlation by Zhukauskas (1972) is widely used to predict the average Nusselt number of the heated cylinder, which is expressed as

$$\overline{Nu} = C\,Re^m Pr^n (Pr/Pr_s)^{1/4}, \qquad (4.8)$$

where the constants C, m and n are tabulated as a function of Reynolds number. All properties (Reynolds number, Re, and Prandtl number, Pr) are evaluated at T_∞ except Pr_s, which is evaluated at T_w.

For a heated cylinder operating in the mixed convection regime, heat transfer from the heated cylinder to the surrounding fluid will involve both forced and free convection. With the idea of free convection being added vectorially to forced convection to study heat transfer from a heated cylinder operating in the mixed convection regime, Hatton, James & Swire (1970) suggested an approach of defining an effective Reynolds number Re_{eff}, which was then used in the forced convection correlation to calculate the heat transfer by mixed convection. Following the approach suggested by Hatton *et al.* (1970), Morgan (1975) derived the following corrections for the prediction of the average Nusselt number of a heated cylinder operating in the mixed convection region:

$$\left.\begin{array}{ll} \text{parallel flow} & \dfrac{\overline{Nu}}{\overline{Nu_F}} = \left(1 + \dfrac{A\,Gr^{m/n}}{Re}\right)^n, \\[2ex] \text{horizontal flow} & \dfrac{\overline{Nu}}{\overline{Nu_F}} = \left(1 + \dfrac{A^2\,Gr^{2m/n}}{Re^2}\right)^{n/2}, \\[2ex] \text{contra flow} & \dfrac{\overline{Nu}}{\overline{Nu_F}} = \left(1 - \dfrac{A\,Gr^{m/n}}{Re}\right)^n, \end{array}\right\} \qquad (4.9)$$
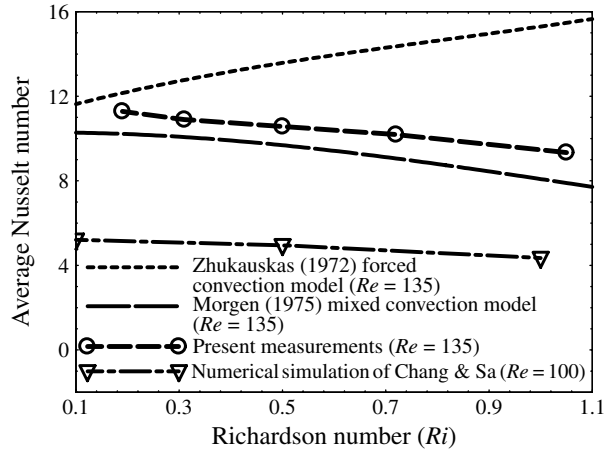
FIGURE 21. Average Nusselt number versus Richardson number.

where $\overline{Nu_F}$ is the Nusselt number for forced convection. The constants A, m and n are tabulated as a function of Gr, Pr and/or Re. For the flow conditions of the present study with contra-flow arrangement, the constants A, m/n and n were set as 0.548, 0.531 and 0.471, respectively, as suggested by Morgan (1975).

Krauce & Tariuk (1985) studied mixed convection from a horizontal cylinder placed in parallel, contra and horizontal air flows. They found that their results agreed with Morgan's (1975) corrections reasonably well for the cases of parallel flow and horizontal flow, but not for contra-flow. They even suggested that the approach of calculating an effective Reynolds number might not work for a heated cylinder placed in a contra-flow.

Figure 21 gives the present measurement results for the variation of the average Nusselt number of the heated cylinder as a function of the Richardson number. The predictions from the empirical models suggested by Zhukauskas (1972) and Morgan (1975) for the present experimental conditions are also given in the figure. We note that the prediction by the Zhukauskas model is shown only for illustrative purposes. This model is applicable to forced convection, and its predictions over the Richardson number range of our experiments, which mostly covers the mixed convection regime, are not expected to be valid. Figure 21 also includes for comparison the numerical results of Chang & Sa (1990) for a cooled cylinder placed in an upward forced flow (i.e. contra-flow arrangement) at a Reynolds number of $Re = 100$.

Figure 21 illustrates that, as expected, the predictions of the Zhukauskas model disagree completely with the experimental estimates of $\overline{Nu}$ in terms of both magnitude and trend. Since the model was developed for forced convection ($Ri \ll 1$), it is not surprising that the difference becomes larger and larger with increasing Richardson number. Once the contributions of buoyancy and free convection have been taken into account, the prediction of the Morgan (1975) model recovers our experimentally measured decreasing trend of the average Nusselt number with increasing Richardson number. Compared with the present experimental data, the Morgan (1975) model was found to underestimate the average Nusselt number slightly. A more precise estimate of the discrepancy is difficult to establish owing to lack of more accurate information on the power loss through the heater ends in the experiment. Similar underestimation of $\overline{Nu}$ by the Morgan model was also reported by Krauce & Tariuk (1985) in their

study of the heat transfer process from a heated cylinder placed in a contra air flow. The numerical results of Chang & Sa (1990) also display the decreasing trend of the Nusselt number with Richardson number, but the actual values are about a factor of 2 smaller than the present experimental data.

5. Concluding remarks

The thermal effects on the wake flow behind a heated circular cylinder operating in the mixed convection regime and exposed to a contra-flow were investigated experimentally. The experiment was conducted in a vertical water channel with the heated cylinder placed horizontally in the middle of the test section and the forced flow approaching the cylinder in a downward direction. By controlling the temperature of the heated cylinder, the corresponding Richardson number was varied between $Ri = 0.0$ (unheated) and $Ri = 1.04$, resulting in a change of the heat transfer process from forced convection to mixed convection. MTV&T was used to achieve qualitative visualization of the thermally induced flow structures and simultaneous quantitative measurements of the velocity and temperature distributions in the wake behind the heated cylinder.

As the Richardson number increased, significant modifications were observed in many characteristics of the flow. They include the wake vortex shedding process and flow pattern, the Strouhal number, the size of the wake recirculation region and wake closure length, and the drag coefficient, among others. Generally speaking, the data were observed to exhibit two distinct regions in behaviour for small ($Ri \leqslant 0.31$) and large ($Ri \geqslant 0.50$) Richardson numbers, with the former being qualitatively similar to the unheated case, and the latter exhibiting significant thermally induced effects.

When the Richardson number was relatively small ($Ri < 0.31$), the wake flow pattern and vortex shedding process exhibited the usual alternate shedding of 'Kármán' vortices at the two sides of the heated cylinder. As the Richardson number became moderate ($0.31 < Ri < 0.72$), the shedding process of the 'Kármán' vortex structures was found to be 'delayed', and took place much farther downstream. When the Richardson number approached unity ($Ri > 0.72$), the alternate shedding of 'Kármán' vortices was replaced by the formation of smaller wake vortices that were generated almost concurrently at two sides of the heated cylinder. The smaller vortices behaved more like 'Kelvin–Helmholtz' vortex structures, and adjacent small vortices were found to merge to form the larger 'Kármán' vortex structures further downstream.

Over the Richardson number range investigated (i.e. from 0.0 to 1.04), the shedding Strouhal number behind the heated cylinder was found to decrease greatly with increasing Richardson number. For relatively small Richardson numbers ($Ri < 0.31$), the wake closure length was found to be slightly shorter than that of the unheated cylinder, but it increased rapidly with increasing Richardson number beyond $Ri > 0.31$. The variations in the size of the wake recirculation region were qualitatively consistent with the expected changes in flow separation that were arrived at using the equivalence of thermally induced effects to a corresponding streamwise pressure gradient over the surface of the heated cylinder. Similar to the behaviour of the wake closure length with Richardson number, the drag coefficient of the heated cylinder was found to become initially slightly smaller than that of the unheated case when the Richardson number was relatively small ($Ri < 0.31$). For relatively large Richardson numbers ($Ri > 0.31$), however, the drag coefficient increased almost linearly with increasing Richardson number. The average Nusselt number ($\overline{Nu}$) was found to decrease almost

linearly with increasing Richardson number in these experiments with the heated cylinder operating in the mixed convection regime and exposed to a contra-flow.

To the authors' knowledge, the work described here represents the first detailed experimental study to investigate the thermal effects on the wake flow behind a heated cylinder operating in the mixed convection regime while placed in a contra-flow. It should be noted that it is quite difficult, if not impossible, to separate out the purely hydrodynamic effects and those connected with the temperature dependence of thermophysical properties based on the measurement results presented here. A numerical study was conducted recently to separate out these effects (Xie, Hu & Ganapathysubramanian 2010). In the numerical study, the simulation results for the case with a constant viscosity (i.e. temperature independent) were compared quantitatively to those with temperature-dependent viscosity under the same flow conditions, while maintaining the same buoyancy effects caused by temperature-dependent density. It was found that the numerical simulations gave very similar results in predicting the wake vortex characteristics and the flow patterns around the heated cylinder as the experimental observations reported in the present study, confirming the dominant role of the hydrodynamic effects. Further details about the numerical study and quantitative comparison with the experimental data are available in Xie *et al.* (2010).

REFERENCES

BADR, H. M. 1983 A theoretical study of laminar mixed convection from a horizontal cylinder in a cross stream. *Intl J. Heat Mass Transfer* **26**, 639–653.

BADR, H. M. 1984 Laminar combined convection a horizontal cylinder – parallel and contra flow regimes. *Intl J. Heat Mass Transfer* **27**, 15–27.

BERGER, E. & WILLE, R. 1972 Periodic flow phenomena. *Annu. Rev. Fluid Mech.* **4**, 313.

BOHL, D. & KOOCHESFAHANI, M. M. 2009 MTV measurements of the vortical field in the wake of an aerofoil oscillating at high reduced frequency. *J. Fluid Mech.* **620**, 63–88.

CHANG, K. S. & SA, J. Y. 1990 The effect of buoyancy on vortex shedding in the near wake of a circular cylinder. *J. Fluid Mech.* **220**, 253–266.

DUMOUCHEL, F., LECORDIER, J. C. & PARANTHOEN, P. 1998 The effective Reynolds number of a heated cylinder. *Intl J. Heat Mass Transfer* **40** (12), 1787–1794.

FERRAUDI, G. J. 1988 *Elements of Inorganic Photochemistry*. Wiley-Interscience.

GENDRICH, C. P. & KOOCHESFAHANI, M. M. 1996 A spatial correlation technique for estimating velocity fields using molecular tagging velocimetry (MTV). *Exp. Fluids* **22** (1), 67–77.

GENDRICH, C. P., KOOCHESFAHANI, M. M. & NOCERA, D. G. 1997 Molecular tagging velocimetry and other novel application of a new phosphorescent supramolecule. *Exp. Fluids* **23**, 361–372.

HARTMANN, W. K., GRAY, M. H. B., PONCE, A. & NOCERA, D. G. 1996 Substrate induced phosphorescence from cyclodextrin–lumophore host–guest complex. *Inorg. Chim. Acta* **243**, 239–248.

HATTON, A. P., JAMES, D. D. & SWIRE, H. W. 1970 Combined forced and nature convection with low speed air flow over horizontal cylinders. *J. Fluid Mech.* **42**, 17–31.

HU, H., JIN, Z., NOCERA, D., LUM, C. & KOOCHESFAHANI, M. 2010 Experimental investigations of micro-scale flow and heat transfer phenomena by using molecular tagging techniques. *Meas. Sci. Technol.* **21** (8) 085401(15pp).

HU, H. & KOOCHESFAHANI, M. M. 2003 A novel technique for quantitative temperature mapping in liquid by measuring the lifetime of laser induced phosphorescence. *J. Vis.* **6** (2), 143–153.

HU, H. & KOOCHESFAHANI, M. M. 2005 The wake behavior behind a heated cylinder in forced and mixed convection regimes. In *ASME Summer Heat Transfer Conference, San Francisco, CA, USA, 17–22 July 2005, ASME-HT2005-72766*.

HU, H. & KOOCHESFAHANI, M. M. 2006 Molecular tagging velocimetry and thermometry (MTV&T) technique and its application to the wake of a heated circular cylinder. *Meas. Sci. Technol.* **17** (6), 1269–1281.

HU, H., LUM, C. & KOOCHESFAHANI, M. M. 2006 Molecular tagging thermometry with adjustable temperature sensitivity. *Exp. Fluids* **40** (5), 753–763.

INCROPERA, F. P. & DEWITT, D. 2001 *Introduction to Heat Transfer*, 4th edn. John Wiley & Sons.

KIEFT, R. N., RINDT, C. C. M. & VAN STEENHOVEN, A. A. 1999 The wake behaviour behind a heated horizontal cylinder. *Exp. Therm. Fluid Sci.* **19**, 193–193.

KOOCHESFAHANI, M. M. 1999 Molecular tagging velocimetry (MTV): progress and applications. *AIAA Paper No.* AIAA-99-3786.

KOOCHESFAHANI, M. M., COHN, R. K., GENDRICH, C. P. & NOCERA, D. G. 1996 Molecular tagging diagnostics for the study of kinematics and mixing in liquid phase flows. In *Proceedings of the 8th International Symposium on Applications of Laser Techniques to Fluid Mechanics, Lisbon, Portugal, 8–11 July 1996*, vol. I, pp. 1.2.1–1.2.12; Also in *Developments in Laser Techniques and Fluid Mechanics, 1997* (ed. R. J. Adrian, D. F. G. Durao, F. Durst, M. V. Heitor, M. Maeda, J. Whitelaw), chapter 2, section 1, p. 125. Springer.

KOOCHESFAHANI, M. M. & NOCERA, D. 2007 Molecular tagging velocimetry. In *Handbook of Experimental Fluid Dynamics* (ed. J. Foss, C. Tropea & A. Yarin), chapter 5.4. Springer.

KRAUCE, J. R. & TARIUK, J. D. 1985 An interferometer study of mixed convection from a horizontal cylinder. In *Proceedings of 23rd National Heat Transfer Conference, Denver, Colorado, 1985*.

MAAS, W. J. P. M., RINDT, C. C. & VAN STEENHOVEN, A. A. 2003 The influence of heat on the 3D-transition of von Kármán vortex street. *Intl J. Heat Mass Transfer* **46**, 3069–3081.

MICHAUX-LEBLOND, N. & BELORGEY, M. 1997 Near wake behaviour of a heated circular cylinder: viscosity–buoyancy duality. *Exp. Therm. Fluid Sci.* **15**, 91–100.

MORGAN, V. T. 1975 The overall heat transfer from smooth circular cylinders. *Adv. Heat Transfer* **11**, 199–264.

NOTO, K., ISHIDA, H. & MATSUMOTO, R. 1985 A breakdown of the Kármán vortex street due to the nature convection. In *Flow Visualization III* (ed. W. J. Yang), pp. 348–352. Springer.

OERTEL, H. Jr 1990 Wakes behind blunt bodies. *Annu. Rev. Fluid Mech.* **22**, 539–564.

OOSTHUIZEN, P. H. & MADAN, S. 1970 Combined convective heat transfer from horizontal cylinders in air. *J. Heat Transfer* **92**, 1194–1196.

OOSTHUIZEN, P. H. & MADAN, S. 1971 The effect of flow direction on combined convective heat transfer from cylinders to air. *J. Heat Transfer* **93**, 240–242.

PARK, H. G., DABIRI, D. & GHARIB, M. 2001 Digital particle image velocimetry/thermometry and application to the wake of a heated circular cylinder. *Exp. Fluids* **30**, 327–338.

PONCE, A., WONG, P. A., WAY, J. J. & NOCERA, D. G. 1993 Intense phosphorescence trigged by alcohol upon formation of a cyclodextrin ternary complex. *J. Phys. Chem.* **97**, 11137–11142.

PRINGSHEIM, P. 1949 *Fluorescence and Phosphorescence*. Interscience.

ROSHKO, A. 1954 On the development of turbulent wakes from vortex streets. NACA Report 1191.

SCHLICHTING, H. 1979 *Boundary-Layer Theory*, 7th edn. McGraw-Hill.

SHAFII, M. B., LUM, C. L. & KOOCHESFAHANI, M. M. 2010 In-situ LIF temperature measurements in aqueous ammonium chloride solution during uni-directional solidification. *Exp. Fluids* **48**, 651–662.

VAN STEENHOVEN, A. A. & RINDT, C. C. M. 2003 Flow transition behind a heated cylinder. *Intl J. Heat Fluid Flow* **24**, 322–333.

THOMSON, S. L. & MAYNES, D. 2001 Spatially resolved temperature measurement in a liquid using laser induced phosphorescence. *J. Fluid Engng* **123**, 293–302.

VÍT, T., REN, M., TRAVNICEK, Z., MARSIK, F. & RINDT, C. C. M. 2007 The influence of temperature gradient on the Strouhal–Reynolds number relationship for water and air. *Exp. Therm. Fluid Sci.* **31**, 751–760.

WANG, A., TRAVNICEK, Z. & CHIA, K. 2000 On the relationship of effective Reynolds number and Strouhal number for the laminar vortex shedding of a heated circular cylinder. *Phys. Fluids* **12** (6), 1401–1410.

WILLIAMSON, C. H. K. 1988 Defining a universal and continuous Strouhal–Reynolds number relationship for the laminar vortex shedding of a circular cylinder. *Phys. Fluids* **31** (10), 2742–2744.

WILLIAMSON, C. H. K. 1996 Vortex dynamics in the cylinder wake. *Annu. Rev. Fluid Mech.* **28**, 477–526.

XIE, Y., HU, H. & GANAPATHYSUBRAMANIAN, B. 2010 Phase transitions in vortex shedding in the wake of a heated circular cylinder at low Reynolds number. In *Proceedings of 47th Annual Technical Meeting of Society of Engineering Science, 3–6 October, 2010, Ames, Iowa.*

ZDRAVKOVICH, M. 1997 *Flow Around Circular Cylinders,* vol. 1. Oxford University Press.

ZHUKAUSKAS, A. 1972 Heat transfer from tubes in cross flow. In *Advances in Heat Transfer* (ed. J. P. Hartnett & T. F. Irvine Jr), vol. 8. Academic.